Article

Discovery Medicine 2025; 37(199): 1677–1698
https://doi.org/10.24976/Discov.Med.202537199.146

GATA4-Overexpressing Dental Pulp Stem Cells Repair Infarcted Myocardium in Acute Myocardial Infarction Rats

Jinxin Lv[1], Yan Wang[2], Yanghong Dong[1], Yi Wu[3], Lu Fu[1,*]

[1]Department of Cardiology, The First Affiliated Hospital of Harbin Medical University, 150008 Harbin, Heilongjiang, China
[2]Department of Cardiology, Heilongjiang Provincial Hospital, 150400 Harbin, Heilongjiang, China
[3]Department of Cardiology, Xianning Central Hospital, 437000 Xianning, Hubei, China
*Correspondence: hydyyxns@163.com (Lu Fu)
Published: 20 August 2025

Background: Adverse cardiac remodeling following acute myocardial infarction (AMI) is one of the leading causes of mortality due to heart failure. This study aims to investigate the efficacy of GATA binding protein 4 (GATA4)-overexpressing dental pulp stem cells (GATA4-DPSCs) in mitigating post-AMI pathological remodeling by exploring their proliferative advantage, paracrine capacity, and cardiac repair potential.

Methods: H9c2 cardiomyocytes co-cultured with GATA4-DPSCs were subjected to hypoxia/reoxygenation (H/R) injury. Cell viability was assessed using Cell Counting Kit-8 (CCK-8) and lactate dehydrogenase release assays. Oxidative stress was detected by malondialdehyde levels and flow cytometry-based reactive oxygen species. Apoptosis was evaluated by Annexin V-fluorescein isothiocyanate/propidium iodide (Annexin V-FITC/PI) staining and Western blotting, whereas cardiomyogenic differentiation markers were analyzed via Western blotting and reverse-transcription quantitative polymerase chain reaction (RT-qPCR). Transcriptomic analysis was also performed. Rat AMI models were established. Cardiac function, myocardial injury, angiogenesis, and myocardial fibrosis markers were evaluated to assess the cardiac repair effect of transplanted GATA4-overexpressing DPSCs post-AMI. Downstream effector proteins of relevant signaling pathways were validated by Western blotting.

Results: *In vitro*, GATA4-DPSCs enhanced antioxidant protection from damage and reduced apoptosis in H9c2 cardiomyocytes post-H/R, while promoting their own cardiomyogenic differentiation. Multi-omics sequencing highlighted the involvement of mitogen-activated protein kinase (MAPK) pathway regulation. *In vivo*, GATA4-DPSCs transplantation improved cardiac function, reduced myocardial damage, enhanced angiogenesis, and ameliorated myocardial fibrosis in AMI rats. This effect correlated with downregulation of MAPK pathway effector proteins.

Conclusions: Transplantation of GATA4-overexpressing DPSCs attenuates post-AMI myocardial remodeling by modulating the MAPK signaling, ultimately mitigating fibrosis and restoring cardiac functional recovery.

Keywords: acute myocardial infarction; dental pulp stem cells; GATA4; apoptosis; angiogenesis; myocardial fibrosis

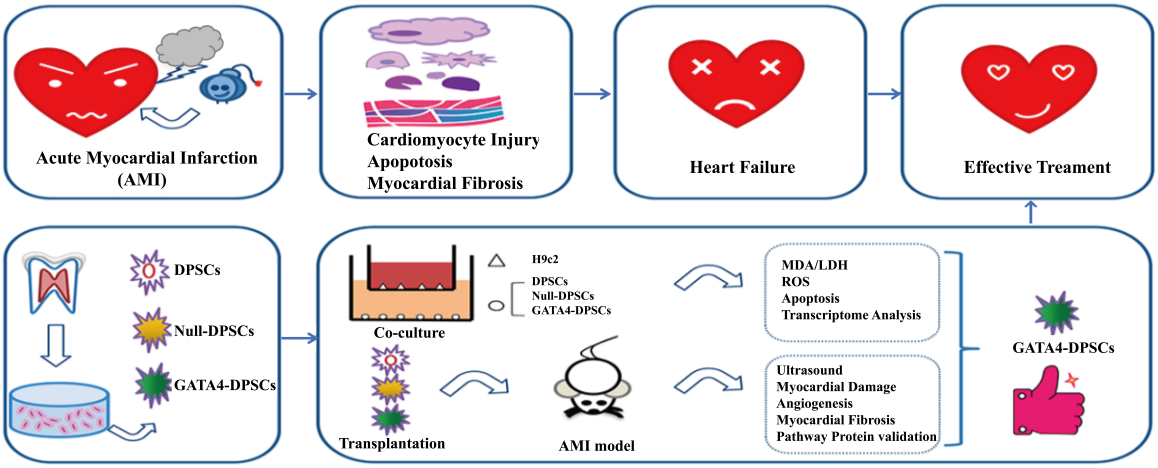

Graphical Abstract

Introduction

Acute myocardial infarction (AMI) is a critical manifestation of coronary artery disease with high mortality risk [1]. Despite therapeutic advances, AMI remains a principal etiology of chronic heart failure [2,3]. Post-AMI pathophysiology involves initial compensatory cardiac hypertrophy, maintaining hemodynamic stability, which progressively transitions to decompensation. This initiates maladaptive ventricular remodeling—characterized by extracellular matrix (ECM) deposition, fibroblast activation, and neurohormonal dysregulation—culminating in functional deterioration [4]. AMI is characterized by progressive fibrosis and structural changes that limit functional recovery. Conventional interventions for the medical condition include pharmacotherapy and revascularization procedures; however, they are unable to regenerate infarcted tissue. Thus, genetically enhanced stem cell therapy emerges as a promising strategy. Dental pulp stem cells (DPSCs) demonstrate distinct advantages, including accessible sourcing with minimal ethical constraints and enhanced proliferative capacity versus bone marrow-derived mesenchymal stem cells (BMSCs; BrdU incorporation: 72% versus 46%; colony formation: 0.22%–0.7% versus 0.024%–0.031%) [5]. GATA binding protein 4 (GATA4), a zinc-finger transcription factor, critically regulates cardiac development [6]. GATA4 demonstrates significant therapeutic potential for myocardial repair through multifaceted mechanisms, including angiogenesis promotion [7], anti-apoptotic activity [8], and precise regulation of hypertrophic pathways [9]. Combined with its established safety profile in cell engineering [10], these properties position GATA4 as a prime candidate for enhancing DPSC-mediated myocardial regeneration.

In this paper, we propose that GATA4-overexpressing DPSCs may facilitate myocardial repair post-AMI by augmenting functional recovery and attenuating pathological remodeling.

Materials and Methods

Identification of DPSCs and the Establishment of GATA4-DPSCs

Isolation and Culture of DPSCs

For DPSC isolation, male Sprague–Dawley (SD) rats (n = 18, aged 8–10 weeks; 250 ± 20 g each) were purchased from Spefu Biotechnology Co., Ltd. (Beijing, China) and housed under standard conditions. Following pentobarbital sodium anesthesia (≥98%, P3761, Sigma-Aldrich, Taufkirchen, Germany; 50 mg/kg, intraperitoneal, i.p.), mandibular and maxillary incisors were aseptically extracted. Postoperative care included dual analgesia by meloxicam (71125-38-7, Sigma-Aldrich, Taufkirchen, Germany; 2 mg/kg, subcutaneous (s.c.)) and buprenorphine (B9275, Sigma-Aldrich, Taufkirchen, Germany; 0.05 mg/kg, s.c. q8–12 h), moistened diet, and hydrogel supplementation for 3 days. After a 7-day recovery period, euthanasia was performed via CO_2 inhalation with cervical dislocation.

Pulp tissue was aseptically dissected, minced, rinsed, centrifuged (1000 ×g, 5 min), and digested with Collagenase I (9001-12-1, Sigma-Aldrich, Taufkirchen, Germany; 3 mg/mL) and Dispase II (42613-33-2, Sigma-Aldrich, Taufkirchen, Germany; 4 mg/mL). Both DPSCs and commercially sourced BMSCs (RAT-iCell-s018, iCell Bioscience, Shanghai, China) were cultured in alpha minimum essential medium (α-MEM) supplemented with 10% fetal bovine serum (FBS) under conditions set at 37 °C and 5% CO_2. Cell morphology was observed via phase-contrast microscopy (Olympus CKX41, Olympus Corporation, Tokyo, Japan), and mycoplasma contamination was confirmed using polymerase chain reaction (PCR; Myco-P-20 kit, Yanxi Biotechnology, Guangzhou, China). In all experiments, DPSCs at passages 3–5 (P3–P5) were utilized.

Surface Marker Characterization of DPSCs by Flow Cytometry

Surface marker expression on DPSCs was analyzed using a flow cytometer (BD FACS Canto II, Becton, Dickinson and Company, Franklin Lakes, NJ, USA). Fluorochrome-conjugated antibodies used in this experiment include: fluorescein isothiocyanate (FITC)-conjugated anti-CD29 (1:10, 11-0291-82, Thermo Fisher Scientific, Waltham, MA, USA), phycoerythrin (PE)-conjugated anti-CD90 (1:10, MA1-80650, Thermo Fisher Scientific, Waltham, MA, USA), allophycocyanin (APC)-conjugated anti-CD31 (1:50, orb1541637, Biorbyt Ltd., Cambridge, UK), and PerCP/Cyanine5.5-conjugated anti-CD45 (1:20, 202220, BioLegend, San Diego, CA, USA). Following antibody incubation (30 min, 4 °C, dark), fluorescence compensation was performed using single-stain controls before sample analysis.

Osteogenic and Adipogenic Differentiation Potential Assay

For osteogenic (21 days) and adipogenic (14 days) induction, DPSCs were treated with specific media: osteogenic medium containing 50 µg/mL ascorbic acid (A8100, Solarbio, Beijing, China), 10 mM β-glycerophosphate (G1485, Solarbio, Beijing, China), and 100 nM dexamethasone (D7770, Solarbio, Beijing, China); adipogenic medium containing 1 µM dexamethasone, 0.5 mM 3-isobutyl-1-methylxanthine (IBMX) (I5879, Sigma-Aldrich, Taufkirchen, Germany), and 10 µg/mL insulin (I9278, Sigma-Aldrich, Taufkirchen, Germany). BMSCs under identical conditions served as the positive group. For osteogenic differentiation analysis, DPSCs were fixed with pre-cooled alkaline phosphatase (ALP) fixative (G1480, Solarbio, Beijing, China; 1 min), incubated in ALP Staining Solution (G1480, Solarbio, Beijing, China) at 37 °C for 15 min, and counterstained with Nuclear Fast Red (G1320, Solarbio, Beijing, China) for 3 min before brightfield microscopy examination (Leica DM750, Leica Microsystems, Wetzlar, Germany). For adipogenic differentiation assessment, cells were fixed in 4% paraformaldehyde (P1110, Solarbio, Beijing, China) for 8 min, treated with 60% isopropanol for 20 s, stained with 0.3% Oil Red O (G1015, Servicebio, Wuhan, China) for 30 min, briefly differentiated in 60% isopropanol for 5 s, washed with distilled water three times for 5 min each, and imaged using brightfield microscopy (Leica DM750, Leica Microsystems, Wetzlar, Germany).

Adenoviral Transduction of GATA4 in DPSCs

Primary DPSCs (P3–P5) were maintained in α-MEM supplemented with 10% FBS and 1% penicillin/streptomycin. For transduction, the cells were seeded in 6-well plates at a density of 5×10^4 cells/well and infected at 70% confluency. Rat GATA4-expressing adenovirus (Ad-GATA4, green fluorescent protein [GFP]-tagged) and empty vector control (Ad-null) were produced by Leaobei Biotech Ltd. (Anhui, China) and purified by means of CsCl gradient centrifugation, with full sequence information provided in **Supplementary Files 1**. Viral titers were diluted to 1×10^8 IFU/mL in complete medium immediately before use. Viral transduction was performed at a multiplicity of infection (MOI) of 50–100 using serum-free medium supplemented with 6 µg/mL polybrene, with incubation for 6 h at 37 °C. Viral titers and MOI were pre-optimized via titration assays.

GATA4 Overexpression Validation by Western Blotting and Reverse-transcription Quantitative PCR (RT-qPCR)

For protein analysis, cell lysates of DPSCs, DPSCs transduced with empty vector (Null-DPSCs) and GATA4-DPSCs groups were prepared using radioimmunoprecipitation assay (RIPA) buffer containing protease inhibitors. Proteins (20 µg/lane) were separated by 10% sodium dodecyl sulfate-polyacrylamide gel electrophoresis (SDS-PAGE), transferred to polyvinylidene difluoride (PVDF) membranes, and probed with GATA4 (1:1000, AF5245, Affinity Biosciences, Nottingham, UK) and glyceraldehyde-3-phosphate dehydrogenase (GAPDH 1:10,000, A19056, ABclonal Technology, Wuhan, China) antibodies, followed by horseradish peroxidase (HRP)-conjugated goat anti-rabbit immunoglobulin G (IgG) secondary antibodies (1:10,000, 31460, Thermo Fisher Scientific, Waltham, MA, USA). Protein signals were detected using enhanced chemiluminescence (ECL) with a Tanon-5200 imaging system (Tanon Science & Technology, Shanghai, China) and quantified using ImageJ software (version 2.16.0, National Institutes of Health, Bethesda, MD, USA).

For mRNA analysis, total RNA was extracted with TRIzol (15596026CN, Thermo Fisher Scientific, Waltham, MA, USA) and reverse-transcribed using Uni All-in-One SuperMix (AU341, TransGen Biotech, Beijing, China). RT-qPCR was performed on an ABI 7300 System (Applied Biosystems, Foster City, CA, USA) using *GAPDH* as reference. Data were analyzed using the instrument's integrated software, i.e., ABI Prism 7300 SDS Software. Relative quantification used the $2^{-\Delta\Delta Ct}$ method: $\Delta Ct = Ct_{GATA4} - Ct_{GAPDH}$; $\Delta\Delta Ct = \Delta Ct_{sample} - \text{mean of} \Delta Ct_{control}$ (DPSCs). Three technical replicates from three biological repeats were analyzed. Primer sequences are provided in **Supplementary Table 1**.

Cell Proliferation and Cytotoxicity Assessment

Cell proliferation was assessed using the Cell Counting Kit-8 (CCK-8) assay. Briefly, cells (5×10^3/well) were seeded in 96-well plates and incubated with CCK-8 reagent (C0038, Beyotime Biotechnology, Shanghai, China) for 2 h for assessments at 0, 24, 48, and 72 h time points. Optical density (OD) was measured at 450 nm (OD_{450}) using a microplate reader (DNM-9602, Pulang New Technology Co.,

Ltd., Beijing, China). CCK-8 reagent is reduced by mitochondrial dehydrogenases in viable cells, producing water-soluble formazan dye. The resulting OD_{450} values directly correlate with viable cell numbers, serving as an indicator of metabolic activity. For cytotoxicity evaluation, lactate dehydrogenase (LDH) activity in culture supernatants was determined using a colorimetric assay (BC0685, Solarbio, Beijing, China) with absorbance measured at 490 nm. Results were calculated based on standard curves.

Hypoxia/Reoxygenation (H/R) Injury in H9c2

Establishment of H/R Model

H9c2 cardiomyocytes (iCell-r012, iCell Bioscience Inc., Shanghai, China) were authenticated by short tandem repeat (STR) profiling (**Supplementary Files 2**) and tested for mycoplasma contamination using PCR (Myco-P-20 kit, Yanxi Biotechnology, Shanghai, China), with full quality control reports in **Supplementary File 3**. Electrophoretic analysis revealed no 500 bp band, which indicates the presence of mycoplasma, verifying mycoplasma-free status (**Supplementary File 4**). H9c2 cells (5×10^4 cells/well) were cultured in 12-well plates for 48 h with untreated, null-transduced, or GATA4-transduced DPSCs (2×10^4 cells/insert) in 0.4 µm Transwell inserts to ensure paracrine-only interaction.

Cells were maintained in Dulbecco's Modified Eagle Medium - High glucose (DMEM-H) (MA0212, Meilunbio, Dalian, China) supplemented with 10% FBS and 1% penicillin-streptomycin (P1400, Solarbio, Beijing, China) for H9c2, while DPSCs were cultured in iCell Primary Mesenchymal Stem Cell Medium (iCell-r012-001b, iCell Bioscience Inc., Shanghai, China). Hypoxia was induced for 6 h in an anaerobic chamber (1% O_2, 94% N_2, 5% CO_2), followed by 6 h reoxygenation (95% air and 5% CO_2). Experimental groups were set up as follows: Control group, H/R group, H/R + DPSCs group, H/R + Null-DPSCs group, and H/R + GATA4-DPSCs group.

Assessment of LDH Release in H9c2 Cells

LDH activity was measured using a commercial kit (BC0685, Solarbio, Beijing, China) following the manufacturer's protocol. After treatments, supernatants from H9c2 cells (96-well plates) were collected. Absorbances (OD value) at 450 nm were measured using a Multiskan FC microplate reader (51119080, Thermo Fisher Scientific, Waltham, MA, USA). The standard curve was generated as: $y = 3.0237x + 0.0352$ (y: LDH concentration in µmol/mL; x: $\Delta A = A_{sample\ well} - A_{background\ control\ well}$). LDH activity was calculated using: LDH activity ($U/10^4$ cells) = $0.133 \times y$, where y was the concentration derived from the standard curve, and 0.133 was the kit-specific conversion factor. OD values are in **Supplementary File 5**.

Malondialdehyde Assay in H9c2 Cells

Malondialdehyde (MDA) content was quantified using a commercial kit (BC0025, Solarbio, Beijing, China). H9c2 cell lysates (96-well plates) were processed according to the manufacturer's protocol. Absorbances at 532 nm and 600 nm were measured using a Multiskan FC microplate reader (51119080, Thermo Fisher Scientific, Waltham, MA, USA). Net absorbance values were calculated: $\Delta A = [(A_{532,\ sample} - A_{532,\ blank}) - (A_{600,\ sample} - A_{600,\ blank})]$. MDA content was determined as: MDA ($nmol/10^4$ cells) = $0.1075 \times \Delta A$, where 0.1075 was the kit-specific coefficient. Raw absorbances are provided in **Supplementary File 6**.

Reactive Oxygen Species Production in H9c2 Cells

Intracellular reactive oxygen species (ROS) levels in H9c2 cells were measured using the fluorescence probe 2′, 7′-dichlorodihydrofluorescein diacetate (DCFH-DA) (ROS Assay Kit, S0033S, Beyotime, Shanghai, China). Flow cytometry was performed using a BD FACSCanto™ II system (Becton, Dickinson and Company, Franklin Lakes, NJ, USA). Data were presented as the percentage of ROS-positive (ROS^+) cells relative to the total gated live cell population.

Cell Viability Assay via CCK-8

Cell viability was assessed by CCK-8 assay (MA0218, Meilunbio, Dalian, China). After adding 10 µL CCK-8 reagent per well and incubating for 2 h at 37 °C. Absorbance was measured at 450 nm using a BioTek Synergy H1 microplate reader (BioTek Instruments, Winooski, VT, USA). OD_{450} values were compared across experimental groups to assess cell viability differences.

Analysis of H9c2 Apoptosis by Flow Cytometry and Western Blotting

Apoptosis was quantified by conducting Annexin V-fluorescein isothiocyanate/propidium iodide (Annexin V-FITC/PI) staining (C1062S, Beyotime, Shanghai, China). Following 24 h reoxygenation, protein lysates from DPSCs, Null-DPSCs, and GATA4-DPSCs were subjected to Western blotting for Bcl-2-associated X protein (Bax, 1:1000, MA1417, APExBIO Technology LLC, Houston, TX, USA), B-cell lymphoma 2 (Bcl-2, 1:1000, T40056, Abmart Inc., Shanghai, China), Desmin (1:10,000, MA5-32068, Thermo Fisher Scientific, Waltham, MA, USA), and Connexin 43 (Cx43, 1:2000, PA5-11632, Thermo Fisher Scientific, Waltham, MA, USA), with GAPDH (1:10,000, A19056, ABclonal Technology, Wuhan, China) as loading control. RT-qPCR (SYBR Green Master Mix, Applied Biosystems, Foster City, CA, USA) quantified T-box transcription factor 3 (*Tbx3*) and NK2 homeobox 5 (*Nkx2.5*) mRNA levels normalized to that of *GAPDH*.

Transcriptomic Analysis of H9c2

H9c2 cells from the control (redefined as Group C), H/R (as Group T1), and H/R + GATA4-DPSCs (as Group T2) groups underwent transcriptome sequencing (Lianchuan Biotech, Hangzhou, China). Differential gene expression analysis was performed using fragments per kilobase of transcript per million mapped reads (FPKM) quantification with a threshold of $|\log_2$ (Fold Change)$| > 1$. Functional enrichment analysis of differentially expressed genes (DEGs) was conducted in R software (version 4.2.2; R Foundation for Statistical Computing, Vienna, Austria) with Bioconductor 3.16 packages, including: ClusterProfiler (version 4.6.2; Bioconductor Core Team, Seattle, WA, USA) for Gene Ontology (GO) and Kyoto Encyclopedia of Genes and Genomes (KEGG) pathway enrichment, org.Rn.eg.db (version 3.16.0; Bioconductor Core Team, Seattle, WA, USA) for *Rattus norvegicus* gene annotation, DOSE (verion 3.24.2; Guangchuang Yu, Southern Medical University, Guangzhou, China) for disease ontology analysis (DisGeNET/Disease Ontology-based), and ggplot2 (version 3.4.0; Hadley Wickham, RStudio, Boston, MA, USA) for visualization. Significant terms were identified with Benjamini–Hochberg adjusted *p*-value (*q*-value) < 0.05, minimum gene set size ≥ 5, and KEGG organism code "rno" for rat-specific pathways.

In Vivo Near-Infrared Imaging for Biodistribution Tracing of GATA4-DPSCs in AMI Rats

Male SD rats (aged 8–10 weeks; 250 ± 20 g each) were obtained from Spefu Biotechnology Co., Ltd. (Beijing, China). AMI was induced in rats by permanent left anterior descending artery (LAD) ligation under echocardiographic guidance (Vevo 3100, FUJIFILM VisualSonics, Toronto, ON, Canada). The sham group underwent thoracotomy without ligation. Rats ($n = 16$, 4 animals per group) were randomized into: (1) NC + i.v. GATA4-DPSCs, (2) NC + i.v. GATA4-DPSCs^{DiR}, (3) AMI + i.p. GATA4-DPSCs^{DiR}, (4) AMI + i.v. GATA4-DPSCs^{DiR}. Anesthetized rats underwent left thoracotomy; LAD was ligated ≈2–3 mm distal to the left atrial appendage (6-0 Prolene suture). Successful AMI was confirmed by myocardial pallor and ST-elevation (>0.2 mV within 24 h) [11]. Five days post-AMI, GATA4-DPSCs/GATA4-DPSCs^{DiR} was injected (via i.v./i.p.). GATA4-DPSCs, labeled with 5 μM lipophilic near-infrared (NIR) fluorescent dye DiR (D12731, Thermo Fisher Scientific, Waltham, MA, USA) for 30 min at 37 °C, were washed with phosphate buffered saline (PBS) and administered to myocardial infarction rats via dual routes: intravenous injection (iv; 1×10^6 cells in 200 μL Ca^{2+}/Mg^{2+}-free DPBS through tail vein, 27G needle, 50 μL/min) or intraperitoneal injection (ip; equal cell dose in 500 μL PBS, 25G needle, 100 μL/min with abdominal massage). At 12 h post-injection, fasted rats (with 8 h of fasting but free access to water) were anesthetized and subjected to whole-body NIR imaging (IVIS Lumina XRMS III, PerkinElmer Inc., Waltham, MA, USA) at excitation/emission wavelengths of 748/780 nm (5 s exposure, FOV 25.4 cm, binning 8) to assess biodistribution. Postoperative penicillin (50,000 IU/kg, A8180, Solarbio, Beijing, China) was administered for 3 days. Anesthesia protocols, postoperative analgesia regimens, and terminal euthanasia procedures were conducted based on the procedures described for DPSC isolation. The homing of GATA4-DPSCs^{DiR} to organs was quantified by net fluorescence intensity (FI). Background signals were determined using the NC + i.v. GATA4-DPSCs group (negative control), and net fluorescence intensity (FI) values were obtained by subtracting these background counts. For the NC + i.v. GATA4-DPSCs^{DiR} group, the net FI in hearts was set as 0 (baseline) for normalization.

Establishment of AMI Model and Cell Transplantation

Rats (n = 30, 6 per group) were purchased from Spefu Biotechnology Co., Ltd. (Beijing, China) and randomized into: (1) Control (sham-operated), (2) AMI + NS, (3) AMI + DPSCs, (4) AMI + Null-DPSCs, and (5) AMI + GATA4-DPSCs. The establishment of the AMI rat model and postoperative infection prevention protocols were consistent with the experimental methods previously described for in vivo tracking of GATA4-DPSCs distribution. At 2 weeks post-AMI induction, the rats received intravenous injections of saline/DPSCs/Null-DPSCs/GATA4-DPSCs (5×10^6 cells) via the tail vein. At 12 weeks post-transplantation, animals were euthanized for endpoint analyses. Blood was collected via cardiac puncture into ethylenediaminetetraacetic acid (EDTA) tubes and centrifuged (2000 ×g, 10 min, 4 °C) for plasma isolation. Heart, liver, lungs, spleen, and kidneys were excised, PBS-rinsed, weighed (organ-to-body weight ratios calculated), and snap-frozen in liquid nitrogen. All animal procedures, including anesthesia, postoperative analgesia, and terminal euthanasia, were conducted according to the protocols established for DPSC isolation.

Echocardiographic Assessment

At the experimental endpoint (12 weeks post-transplantation), cardiac function was compared across five groups. Under isoflurane anesthesia (1.5%–2% in O_2), the rats underwent terminal echocardiography using a Vevo 3100 small-animal imaging system (FUJIFILM VisualSonics, Toronto, ON, Canada) with continuous electrocardiogram (ECG) monitoring and ventilatory support (60–80 breaths/min). Core temperature was maintained at 37 °C. Left ventricular parameters were measured from B-mode and M-mode images, with data averaged across three consecutive cardiac cycles.

Serum ELISA

Serum levels of troponin T (TnT), creatine kinase-MB (CKMB), basic fibroblast growth factor (bFGF), and vascular endothelial growth factor (VEGF) levels were measured using species-specific enzyme-linked immunosorbent assay (ELISA) kits (TnT ELISA Kit: ZK-R3467, Ziker Biological Technology, Shanghai, China; CKMB ELISA kit: ml107008, mlbio, Shanghai, China; bFGF: ml107060, mlbio, Shanghai, China; VEGF: ml106795, mlbio, Shanghai, China), Absorbance (450 nm) was read on a microplate reader (iMark, Bio-Rad Laboratories, Hercules, CA, USA). Standard curves were generated from reference standards after blank subtraction. Analyte concentrations were interpolated from standard curves and multiplied by dilution factors: TnT, 5 × (10 µL serum + 40 µL diluent); CKMB/bFGF/VEGF, 2 × (50 µL serum + 50 µL diluent). All ELISA experiments were performed in accordance with kit protocols.

Histological Staining

Myocardial, pulmonary, hepatic, splenic, and renal tissues were fixed, paraffin-embedded, sectioned (4 µm), and stained with hematoxylin and eosin for histopathological evaluation (Olympus BX53, Olympus Corporation, Tokyo, Japan).

Fibrosis Assessment by Masson's Trichrome Staining

Paraffin-embedded rat myocardial sections were deparaffinized, rehydrated, and stained with Masson's trichrome (G1006-20ML, Servicebio, Wuhan, China) using the following reagents: Weigert's hematoxylin for staining nuclei, Biebrich scarlet-acid fuchsin for staining cytoplasm/muscle, and aniline blue for staining collagen. Collagen deposition (blue), cardiomyocytes (red), and nuclei (dark blue) were visualized by brightfield microscopy (Leica DM750, Leica Microsystems, Wetzlar, Germany). Fibrosis was quantified as collagen volume fraction (%) using ImageJ software (version 2.16.0, National Institutes of Health, Bethesda, MD, USA).

Immunohistochemical Analysis of Collagen Deposition

Paraffin sections were subjected to citrate-based antigen retrieval (121 °C, 20 min, high-pressure), blocking with 5% bovine serum albumin (BSA; 37 °C, 30 min), and incubation with primary antibodies against collagen I (1:100, AF7001, Affinity Biosciences Ltd., Nottingham, UK) and collagen III (1:100, AF5457, Affinity Biosciences Ltd., Nottingham, UK) at 4 °C overnight. After applying HRP-conjugated goat anti-rabbit IgG (1:10,000, 31460, Thermo Fisher Scientific, Waltham, MA, USA) at 37 °C for 30 min, 3,3′-diaminobenzidine (DAB) development (3–5 min) was halted by distilled water. The sections were counterstained with hematoxylin for 3 min, dehydrated through a gradient of ethanol solutions, cleared in xylene, and mounted with neutral resin (CW0136, CWBIO, Beijing, China). The Olympus BX53 microscope (Olympus Corporation, Tokyo, Japan) was used for imaging.

Expression of Key Differentially Expressed Proteins and Pathway-Related Proteins by Western Blotting

Myocardial tissues were homogenized in ice-cold RIPA buffer (89901, Thermo Fisher Scientific, Waltham, MA, USA) supplemented with protease/phosphatase inhibitors and subsequently centrifuged at 12,000 $\times g$ and 4 °C for 30 min. The Western blot analysis was performed following the previously described methodology, using the following primary antibodies targeting: heat shock protein 70 (HSP70, 1:1000, K200048M, Solarbio, Beijing, China), Neuropeptide Y (Npy; 1:1000, A3178, ABclonal Technology, Wuhan, China); proline/arginine-rich end leucine-rich repeat protein (Prelp; 1:1000, A18573, ABclonal Technologyl, Wuhan, China); Creb/p-Creb (1:1000; 9197/9198, CST, Danvers, MA, USA); Nuclear factor-κB (NF-κB) and phosphorylated NF-κB (p-NF-κB) (1:1000, 8242/3033, CST, Danvers, MA, USA); and GAPDH (1:10,000, A19056, ABclonal Technologyl, Wuhan, China). Additionally, the anti-HSP70 antibody targets multiple isoforms, including Hspa1a and Hspa1b, as well as other subtypes. HRP-conjugated goat anti-mouse IgG (1:1000, SE131, Solarbio, Beijing, China) was employed as the corresponding secondary antibody for HSP70, whereas HRP-conjugated goat anti-rabbit IgG (1:10,000, 31460, Thermo Fisher Scientific, Waltham, MA, USA) was utilized for the remaining targets.

Statistical Methods

ImageJ software (version 2.16.0, National Institutes of Health, Bethesda, MD, USA), GraphPad Prism software (version 8.0, GraphPad Software, Inc., San Diego, CA, USA), and R software (version 4.2.2; R Foundation for Statistical Computing, Vienna, Austria) were used for graphing and statistical analysis. Data are expressed as mean ± standard deviation. Parametric statistical analyses were performed under the assumption of normality and homogeneity of variance. Normality was assessed using the Shapiro–Wilk test ($p \geq 0.05$), and homogeneity of variance was confirmed via Levene's test ($p \geq 0.05$). Comparisons between two groups were conducted with Student's *t*-test, while one-way analysis of variance (ANOVA) followed by Tukey's *post hoc* test was applied for multi-group comparisons. Non-normally distributed data were analyzed using the Mann–Whitney *U* test (two groups) or the Kruskal–Wallis test with Dunn's correction (multiple groups). A difference with $p < 0.05$ was considered statistically significant.

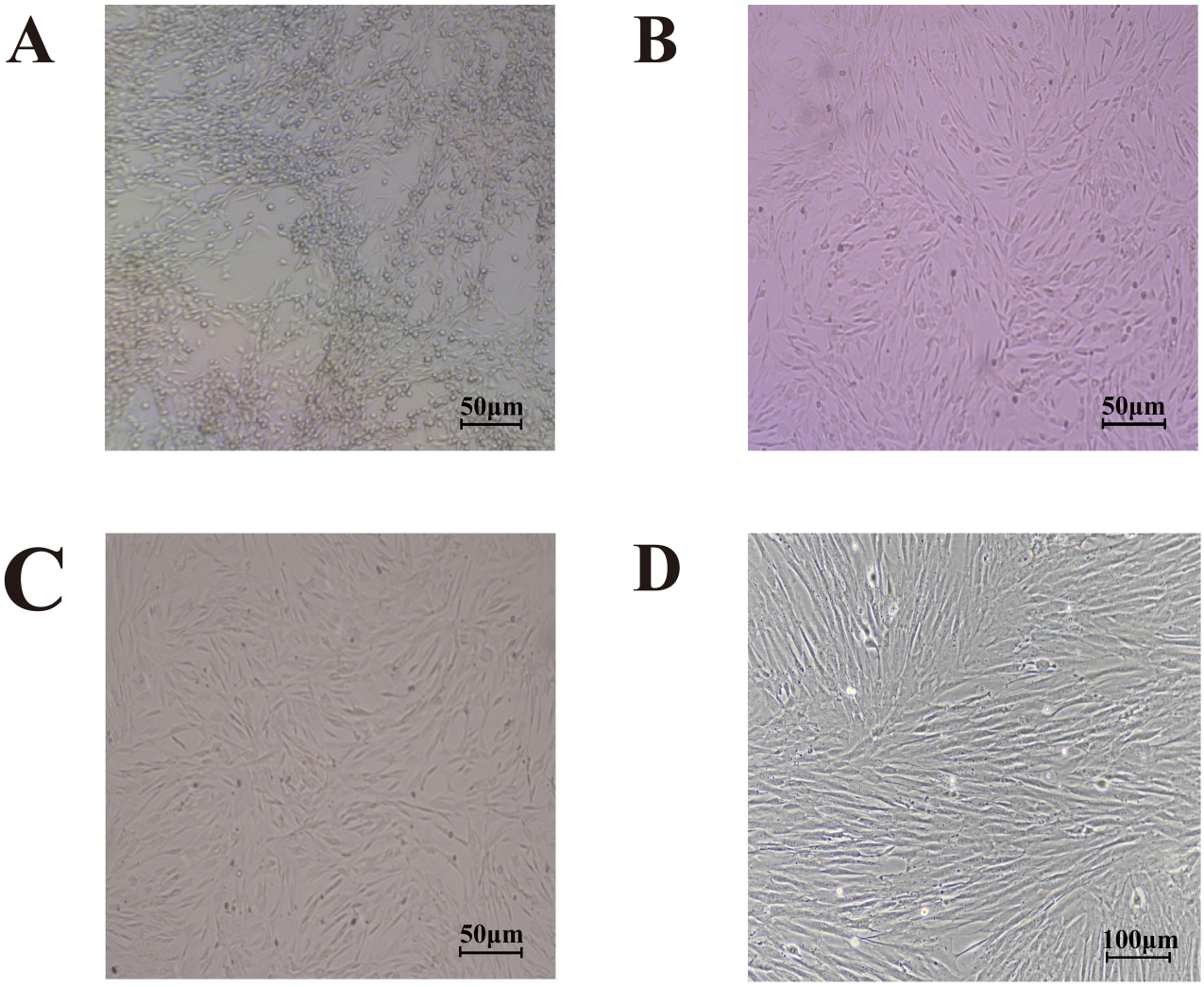

Fig. 1. Morphological characterization of DPSCs. (A) Primary DPSCs exhibited characteristic adherent growth patterns, demonstrating typical cobblestone-like morphology typical of MSCs. (B) P3 DPSCs transitioned to homogeneous spindle-shaped morphology, indicating activated proliferative capacity under standard culture conditions. (C) P5 DPSCs showed elongated fibroblastoid morphology with parallel alignment and whorl-like growth patterns, confirming stable MSC characteristics. Scale bar (A–C) = 50 μm. (D) P1 BMSCs showed characteristic spindle-shaped morphology and parallel alignment. Scale bar (D) = 100 μm. Abbreviations: DPSCs, dental pulp stem cells; BMSC, bone marrow-derived mesenchymal stem cells.

Results

Morphological Features and Mycoplasma-Free Status of DPSCs and BMSCs

Primary DPSCs exhibited typical MSC cobblestone-like morphology during initial expansion (Fig. 1A). Under serial passaging, P3 DPSCs transitioned to a homogeneous spindle-shaped morphology (Fig. 1B), while P5 DPSCs showed elongated fibroblastoid cells with parallel alignment and whorl-like patterns (Fig. 1C). P1 BMSCs displayed a spindle-shaped morphology in parallel arrays (Fig. 1D). All BMSCs and DPSCs cultures tested negative for mycoplasma contamination (**Supplementary File 7 and Supplementary File 8**).

Validation and Phenotype of GATA4-DPSCs

Flow cytometric analysis (Fig. 2A) confirmed that cultured rat DPSCs expressed characteristic MSC surface markers CD29 and CD90 (>95% positivity), while remaining negative for pan-leukocyte marker CD45 and endothelial marker CD31 (<2% positivity). This immunophenotypic profile aligns with the established MSC criteria [12,13].

ALP staining revealed distinct alkaline phosphatase activity deposition (visualized as blue staining) in osteogenically induced DPSCs (Fig. 2B), while BMSCs (positive control) exhibited more intense and homogeneous ALP signal distribution (stronger blue staining; Fig. 2C). Similarly, Oil Red O staining demonstrated red-stained lipid

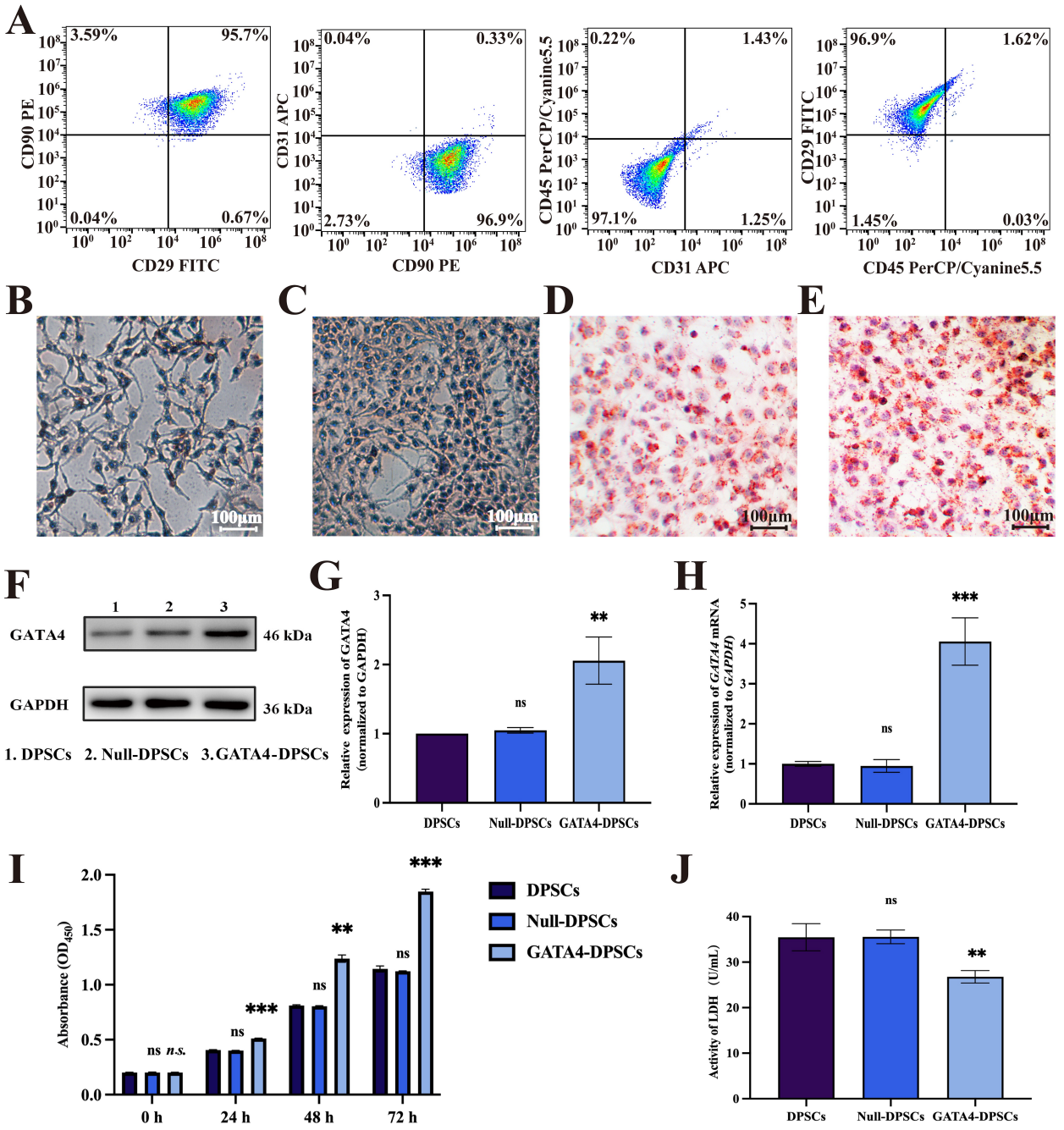

Fig. 2. Characterization of DPSCs and GATA4-DPSCs. (A) Flow cytometric analysis of DPSCs specific antigenic markers ($CD29^+/CD90^+/CD31^-/CD45^-$). (B–E) Multilineage differentiation potential: (B) ALP activity deposition (blue staining) in DPSCs; (C) Positive control for osteogenic differentiation; (D) Lipid droplets in DPSCs; (E) Positive control for adipogenic differentiation. Scale bar (B–E) = 100 μm. (F–H) GATA4 overexpression validation: (F) Representative Western blots (46 kDa band); (G) Quantified protein expression normalized to GAPDH; (H) mRNA expression of *GATA4* by RT-qPCR normalized to *GAPDH*; (I) Cell viability (CCK-8 assay) at indicated time points post-transfection. (J) Cytotoxicity assessment by LDH release. $^{ns}p \geq 0.05$ versus DPSCs group; $^{n.s.}p \geq 0.05$, $^{**}p < 0.01$, $^{***}p < 0.001$ versus Null-DPSCs group. $n = 3$. Abbreviations: DPSCs, dental pulp stem cells; LDH, lactate dehydrogenase; ALP, alkaline phosphatase; RT-qPCR, reverse-transcription quantitative polymerase chain reaction; CCK-8, Cell Counting Kit-8; GAPDH, glyceraldehyde 3-phosphate dehydrogenase.

droplets in adipogenically induced DPSCs (Fig. 2D), contrasting with extensive lipid deposition in BMSCs (positive control, Fig. 2E).

Western blot analysis revealed significantly stronger band intensity in GATA4-DPSCs compared to Null-DPSCs with corresponding elevation in relative density ($p < 0.01$;

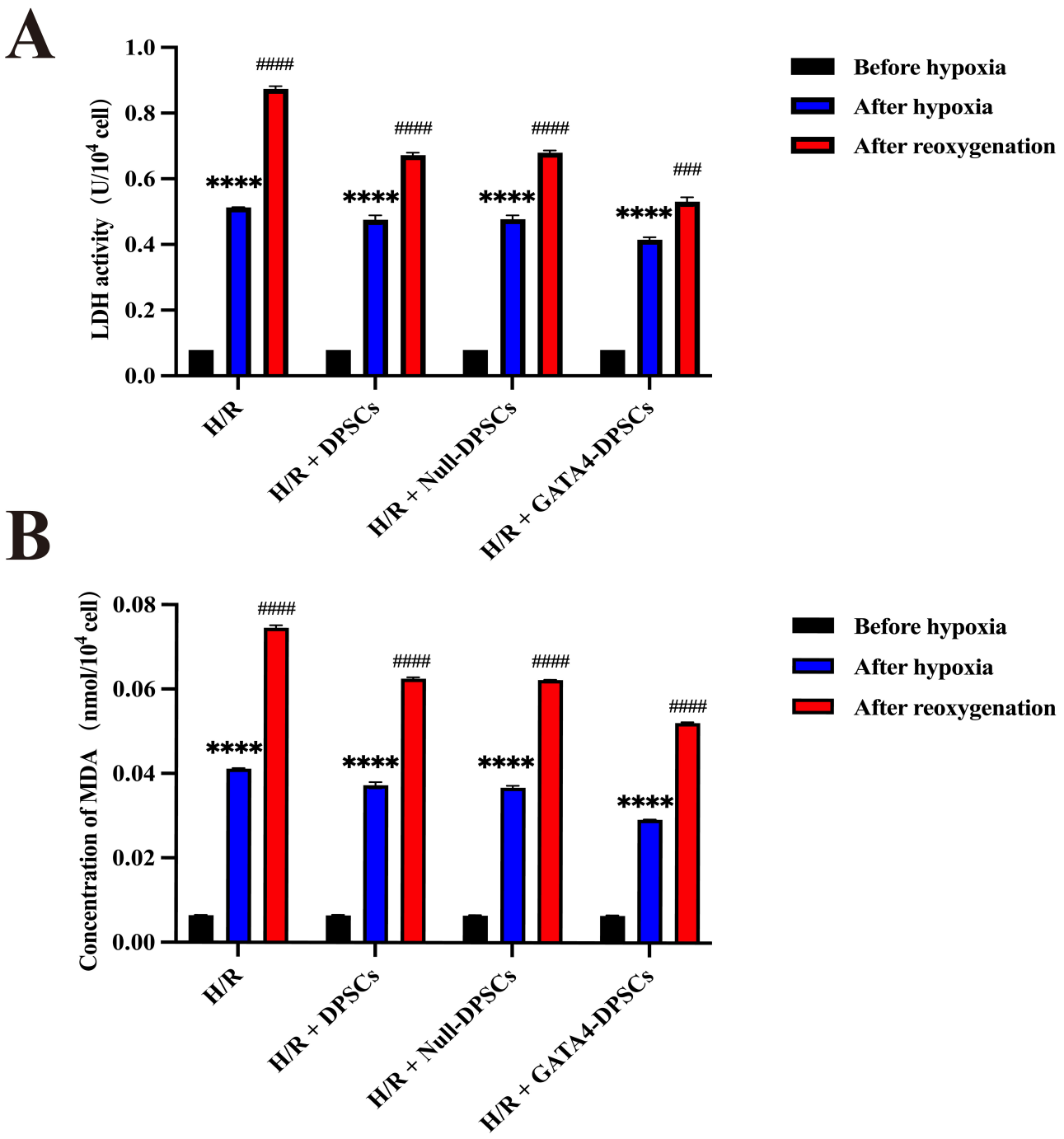

Fig. 3. Successful establishment of an H/R injury model. (A) LDH release levels in all groups at different conditions (before hypoxia, after hypoxia, and after reoxygenation). (B) MDA contents at different conditions. ****$p < 0.0001$ versus before hypoxia; $^{###}p < 0.001$, $^{####}p < 0.0001$ versus after hypoxia. $n = 3$ biological replicates per group. Abbreviations: DPSCs, dental pulp stem cells; H/R, hypoxia/reoxygenation; LDH, lactate dehydrogenase; MDA, malondialdehyde.

Fig. 2F,G). RT-qPCR confirmed markedly upregulated *GATA4* mRNA levels in the GATA4-DPSCs group versus the Null-DPSCs group ($p < 0.001$; Fig. 2H).

The CCK-8 assay results demonstrated time-dependent differences in cellular proliferation among the experimental groups (Fig. 2I). The raw OD_{450} values directly reflected cellular metabolic activity. Baseline measurements at 0 h showed comparable metabolic activity across all groups ($p \geq 0.05$), confirming consistent cell seeding. GATA4-DPSCs exhibited significantly enhanced proliferation compared to Null-DPSCs at all subsequent time points (24 h: $p < 0.001$; 48 h: $p < 0.01$; 72 h: $p < 0.001$), reaching a 1.64-fold increase in metabolic activity by 72 h. This robust proliferative advantage strongly

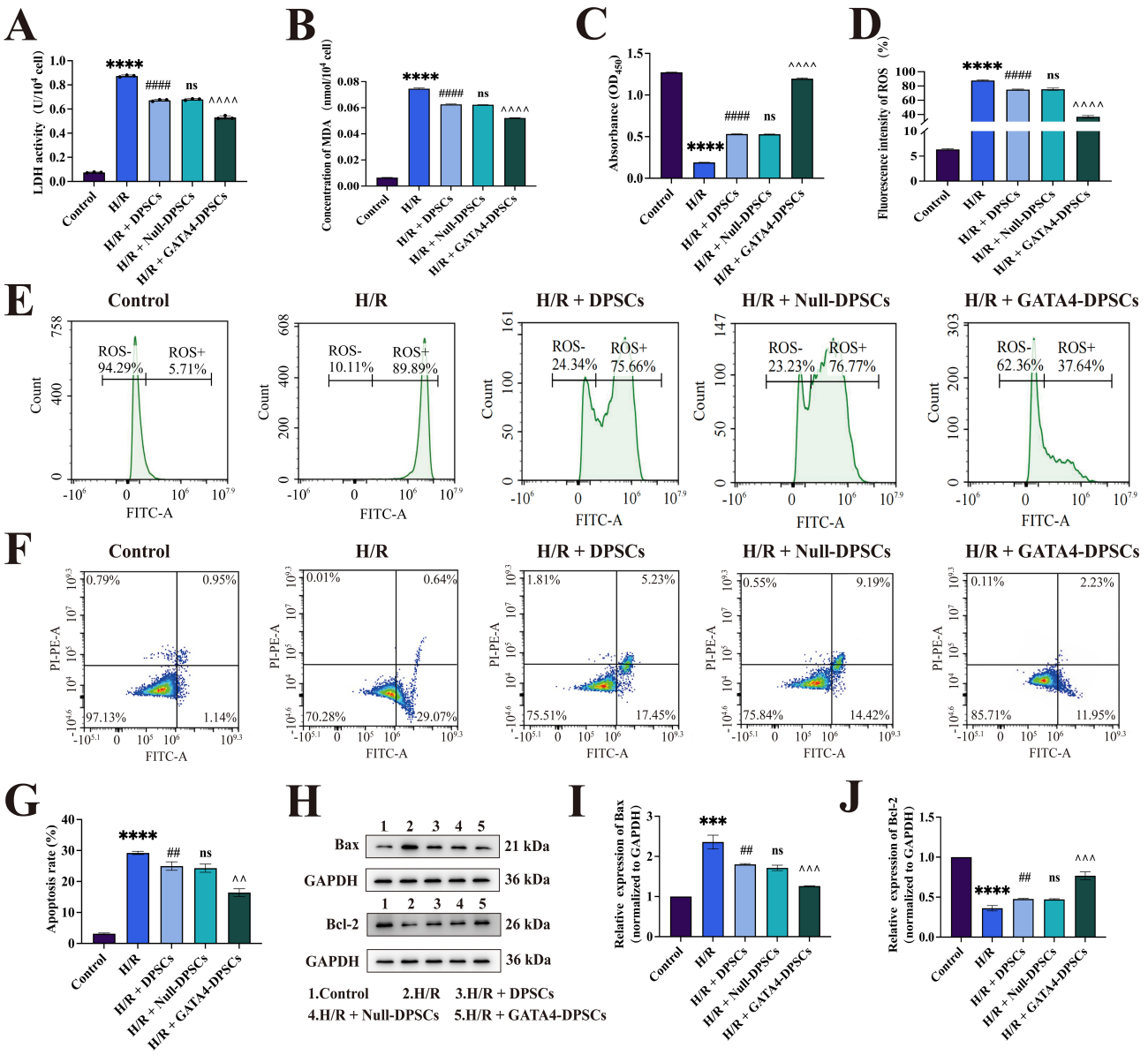

Fig. 4. Protective effects of GATA4-DPSCs co-culture against H/R injury in H9c2 cardiomyoblasts. (A) LDH release levels. (B) MDA content. (C) Cell viability was measured by the CCK-8 assay. (D,E) Intracellular ROS levels (D: quantitative analysis; E: representative images). (F,G) Apoptosis analysis by Annexin V-FITC/PI staining (F: flow cytometry plots; G: quantitative results). (H–J) Western blot analysis of apoptosis-related proteins (H: representative Western blots; I: Bax/GAPDH; J: Bcl-2/GAPDH ratio). ***$p < 0.001$, ****$p < 0.0001$ versus Control; $^{\#\#}p < 0.01$, $^{\#\#\#\#}p < 0.0001$ versus H/R; $^{ns}p \geq 0.05$ versus H/R + DPSCs; $^{\wedge\wedge}p < 0.01$, $^{\wedge\wedge\wedge}p < 0.001$, $^{\wedge\wedge\wedge\wedge}p < 0.0001$ versus H/R + Null-DPSCs. $n = 3$ independent experiments. Abbreviations: DPSCs, dental pulp stem cells; H/R, hypoxia/reoxygenation; LDH, lactate dehydrogenase; MDA, malondialdehyde; ROS, reactive oxygen species; Annexin V-FITC/PI, Annexin V-fluorescein isothiocyanate/propidium iodide.

suggests that GATA4 overexpression promotes DPSC expansion. Importantly, DPSCs and Null-DPSCs maintained similar rates ($p \geq 0.05$ at all time points), confirming the viral vector's safety profile. The GATA4-DPSCs group exhibited lower LDH activity than the Null-DPSCs group ($p < 0.01$; Fig. 2J), suggesting that GATA4 may reduce DPSCs' metabolic stress, with no significant cytotoxicity observed in any group throughout the culture period.

H/R-Induced Cellular Injury and Apoptosis

Hypoxia significantly increased LDH (Fig. 3A) and MDA (Fig. 3B) levels of H9c2 in all groups, and these markers were further elevated following reoxygenation, confirming the successful establishment of the H/R injury model.

Notably, co-culture with GATA4-DPSCs significantly attenuated H/R-induced elevations in both LDH ($p <$

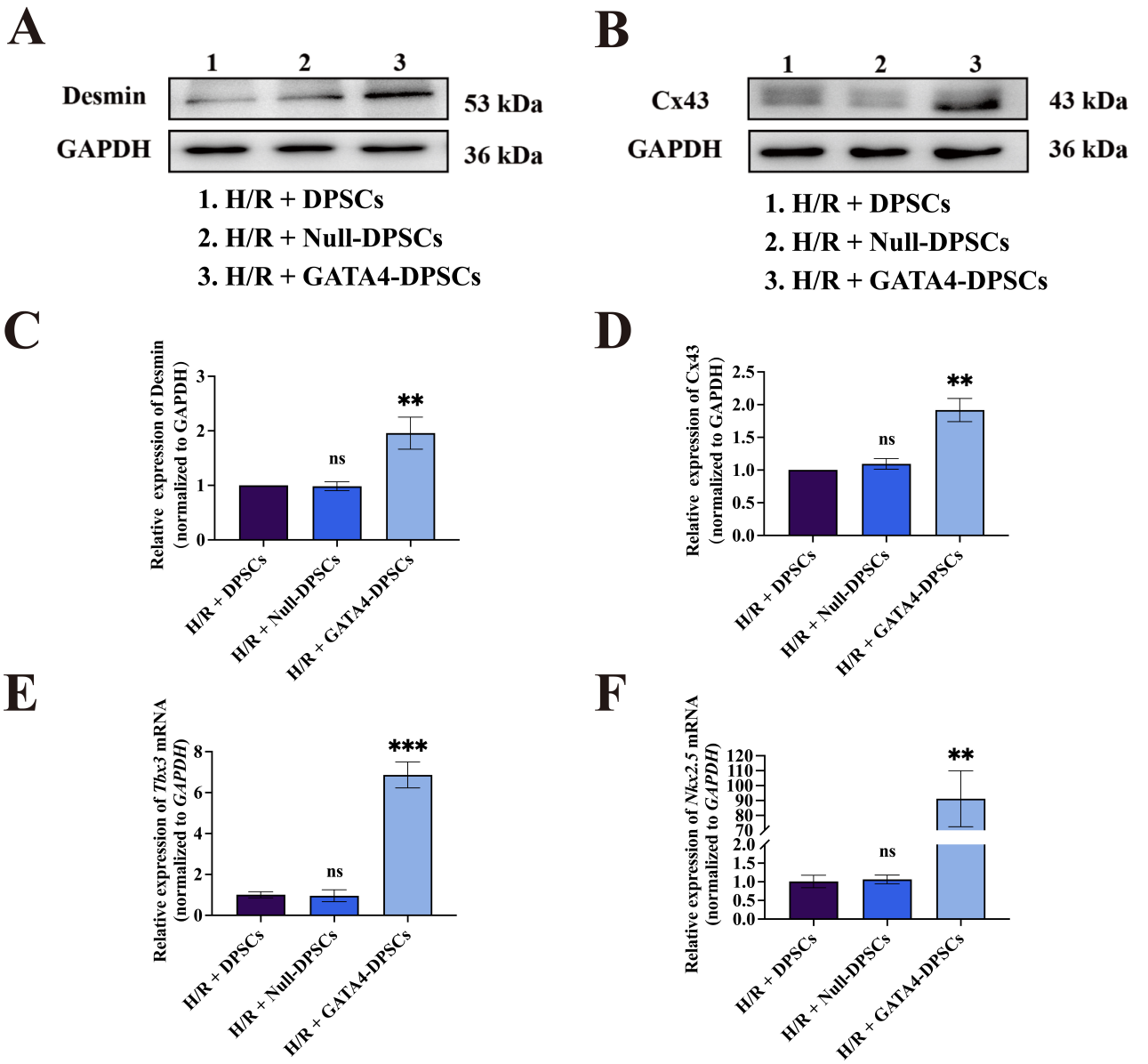

Fig. 5. GATA4-DPSCs upregulates cardiac-specific proteins and associated transcriptional factors. Representative Western blots of Desmin (A) and Cx43 (B). Quantitative analysis of Desmin/GAPDH (C) and Cx43/GAPDH (D). *GAPDH*-normalized mRNA expression levels of cardiac transcription factors *Tbx3* (E) and Nkx2.5 (F) measured by RT-qPCR. $^{ns}p \geq 0.05$ versus H/R + DPSCs; $^{**}p < 0.01$, $^{***}p < 0.001$ versus H/R + Null-DPSCs. $n = 3$. Abbreviations: DPSCs, dental pulp stem cells; H/R, hypoxia/reoxygenation.

0.0001; Fig. 4A) and MDA ($p < 0.0001$; Fig. 4B) levels in H9c2 cells compared with Null-DPSCs co-culture.

CCK-8 assay revealed that H/R injury significantly reduced cell viability versus the Control group ($p < 0.0001$, Fig. 4C). All DPSCs-treated groups (DPSCs, Null-DPSCs, and GATA4-DPSCs) showed improved viability compared to the H/R group, with GATA4-DPSCs demonstrating the most potent protective effect ($p < 0.0001$ versus Null-DPSCs; Fig. 4C). Consistently, GATA4-DPSCs co-culture yielded the lowest ROS levels among all treatment groups ($p < 0.0001$ versus Null-DPSCs; Fig. 4D,E).

As key regulators of mitochondrial apoptosis, Bax promotes cytochrome c release by forming pores in the outer mitochondrial membrane, while Bcl-2 inhibits this process by sequestering Bax [14]. Our data demonstrated that all DPSCs-treated groups (DPSCs, Null-DPSCs, and GATA4-DPSCs) exhibited an anti-apoptosis effect, with the GATA4-DPSCs showing the most pronounced impact ($p <$ 0.01 versus H/R + Null-DPSCs, Fig. 4F,G). H/R treatment significantly upregulated pro-apoptotic Bax while downregulating anti-apoptotic Bcl-2. These molecular changes correlated with the observed apoptosis severity, where H/R + GATA4-DPSCs displayed maximal cytoprotection (Fig. 4H–J).

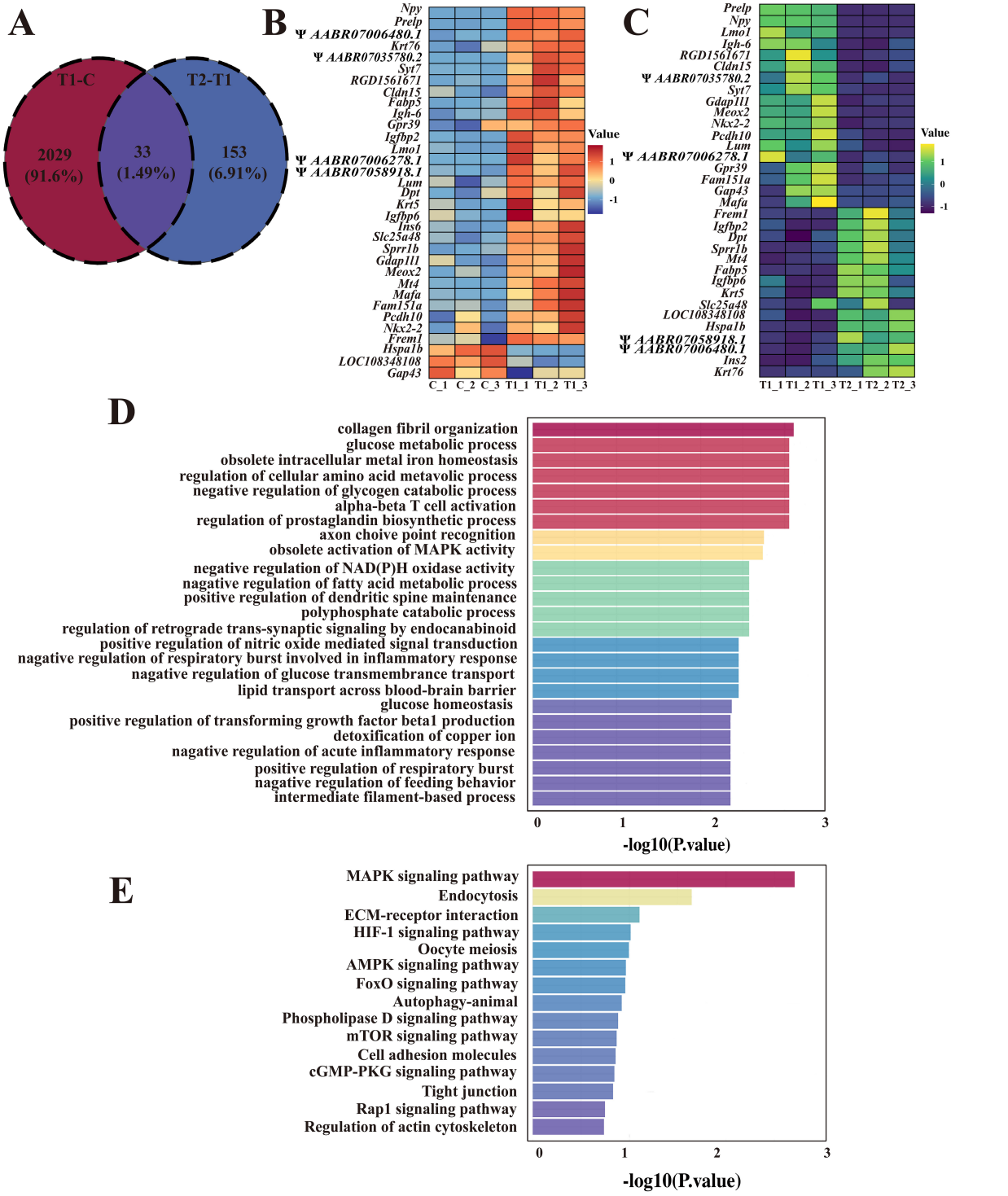

Fig. 6. Transcriptomic profiling reveals core therapeutic targets. (A) Venn diagram identifying 33 intersecting DEGs ($|\log_2 FC| > 1$, q value < 0.05). (B) Heatmaps display Z-score-normalized expression of 33 overlapping DEGs in T1-C group (disease signature), with red boxes indicating upregulated genes and blue boxes marking downregulated genes. (C) Heatmaps display Z-score-normalized expression of 33 overlapping DEGs in T2-T1 group (treatment response), with green boxes indicating upregulated genes and purple boxes marking downregulated genes. Protein-coding genes in standard symbols (e.g., *Npy*) are shown on the Y-axis, with pseudogenes labeled with database accession numbers (e.g., *AABR07013255.1*) and marked with Ψ. (D) Top enriched GO terms for intersecting DEGs. (E) Significant KEGG pathways enriched in intersecting DEGs. Abbreviations: DEGs, differentially expressed genes; GO, gene ontology; KEGG, Kyoto Encyclopedia of Genes and Genomes.

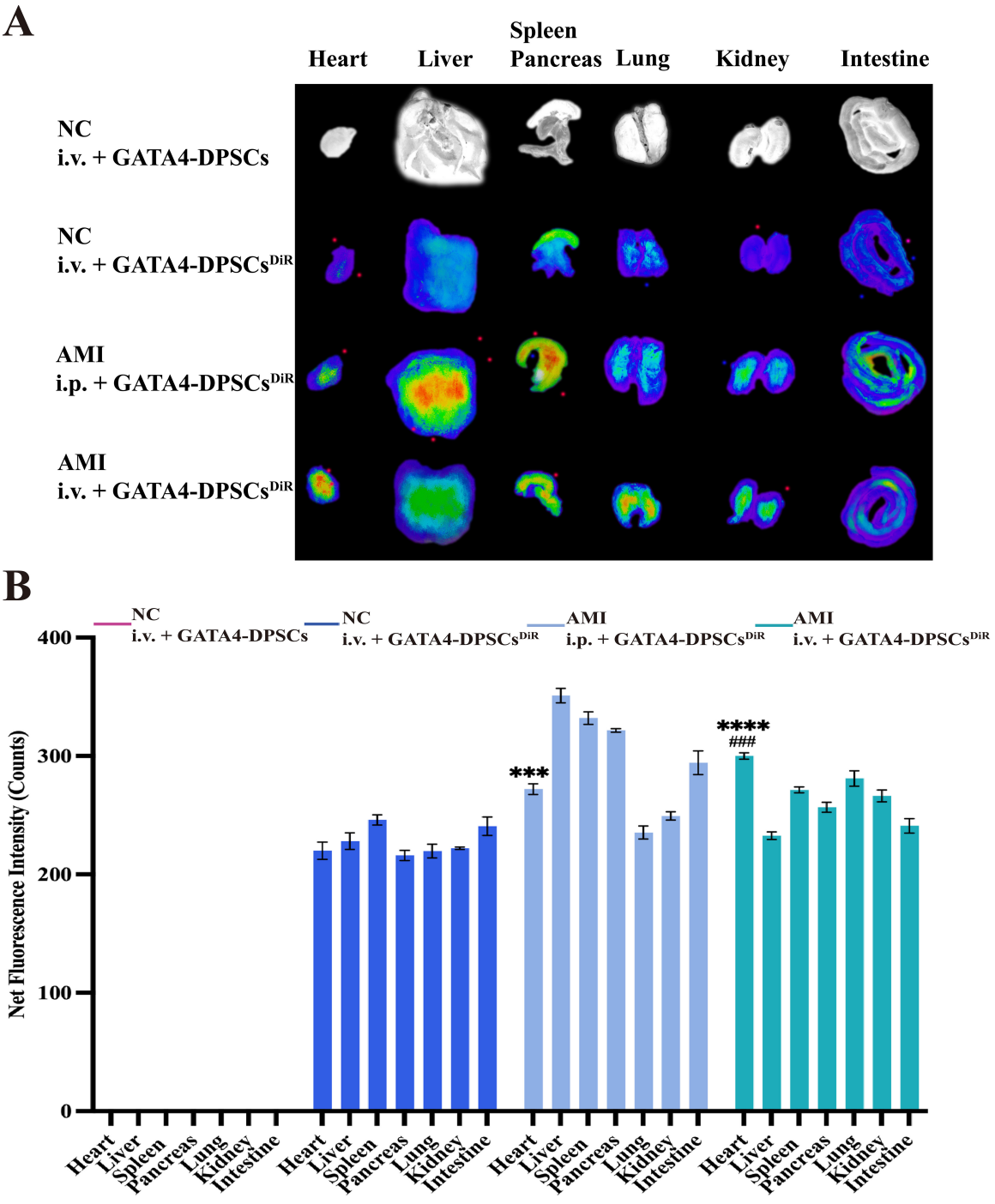

Fig. 7. Fluorescence distribution of DiR-labeled GATA4-DPSCs in organs *ex vivo*. (A) *Ex vivo* organ imaging of the major organs in AMI model rats by near-infrared fluorescence (NIRF). (B) Quantification of GATA4-DPSCs^{DiR} homing to organs. Mean counts in the NC + i.v. GATA4-DPSCs group (background noise): Heart = 14, Liver = 11, Spleen = 10, Pancreas = 14, Lung = 14, Kidney = 10, Intestine = 10. In the NC + i.v. GATA4-DPSCs^{DiR} group, net FI counts were normalized to 0 (baseline). ***$p < 0.001$, ****$p < 0.0001$ versus hearts in NC + i.v. GATA4-DPSCs^{DiR}; $^{\#\#\#}p < 0.001$ versus hearts in NC + i.p. GATA4-DPSCs^{DiR}. $n = 4$ per group. Abbreviations: AMI, acute myocardial infarction; DPSCs, dental pulp stem cells; FI, fluorescence intensity.

Cardiomyogenic Differentiation of DPSCs

Dysregulation of Desmin and Cx43 is associated with arrhythmias and impaired contractility in ischemic heart disease [15,16]. The dysregulation of Tbx3 and Nkx2.5 is implicated in congenital heart defects and post-infarction remodeling [17,18]. GATA4-DPSCs co-culture significantly upregulated cardiac markers Desmin and Cx43 compared to Null-DPSCs co-culture (both $p < 0.01$; Fig. 5A–

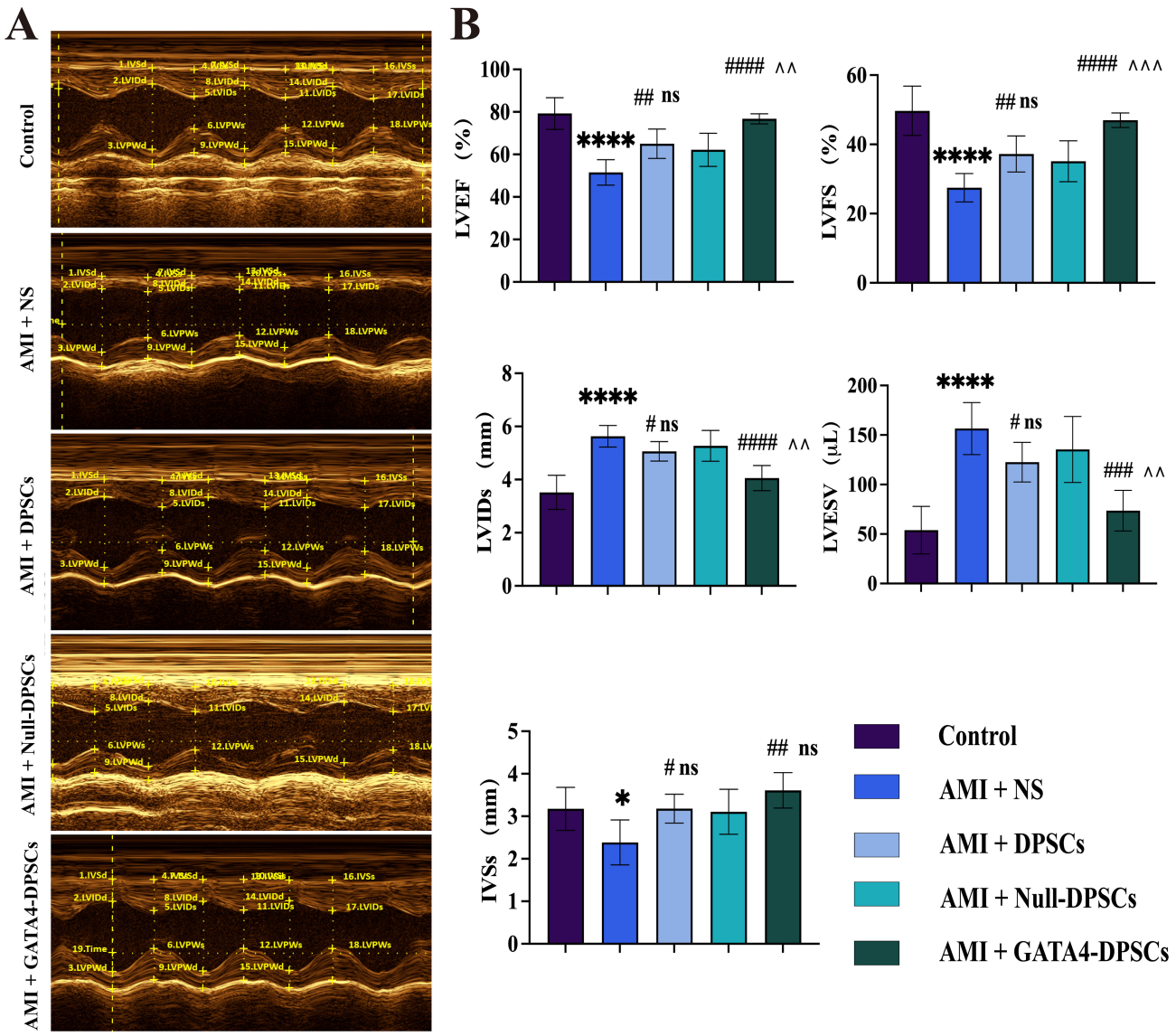

Fig. 8. Echocardiographic assessment of cardiac function. (A) Representative echocardiograms. (B) Quantitative analysis of systolic function (LVEF, LVFS), ventricular remodeling (LVIDs, LVESV), and wall thickness (IVSs). $^{*}p < 0.05$, $^{****}p < 0.0001$ versus Control; $^{\#}p < 0.05$, $^{\#\#}p < 0.01$, $^{\#\#\#}p < 0.001$, $^{\#\#\#\#}p < 0.0001$ versus AMI + NS; $^{ns}p \geq 0.05$, $^{\wedge\wedge}p < 0.01$, $^{\wedge\wedge\wedge}p < 0.001$ versus AMI + Null-DPSCs. $n = 6$. Abbreviations: AMI, Acute myocardial infarction; LVEF, left ventricular ejection fraction; LVESV, left ventricular end-systolic volume; LVFS, left ventricular fractional shortening; LVIDs, left ventricular internal diameter in systole; IVSs, Interventricular septal thickness at end-systole.

D). Correspondingly, cardiac transcription factors *Tbx3* ($p < 0.001$) and *Nkx2.5* ($p < 0.01$; Fig. 5E,F) were coordinately elevated, with all data normalized to *GAPDH*.

Transcriptome Profiling of H9c2

FPKM-based analysis of DEGs ($|\log_2 FC| > 1$, $p < 0.05$) identified 33 common genes shared between Group T1 vs. C (disease-associated) and Group T2 vs. T1 (therapy-responsive) comparisons (**Supplementary Table 2**), as illustrated in the Venn diagram (Fig. 6A). Distinct expression patterns were visualized by hierarchical clustering in the heatmaps. Group T1 versus C: Genes encoding ECM structural components (e.g., *Prelp*) were significantly upregulated (red cluster), suggesting ECM remodeling under H/R treatment. Conversely, oxidative stress-responsive related proteins (e.g., *Hspa1b*) were downregulated (blue cluster), indicating impaired cellular stress defense (Fig. 6B). In the Group T2 versus T1 comparison, the expression of oxidative stress-responsive related proteins (e.g., *Hspa1b*) was partially restored (green cluster), suggesting a mitigation of T1-induced cellular damage. Concurrently, ECM-related genes (e.g., *Prelp*) showed de-

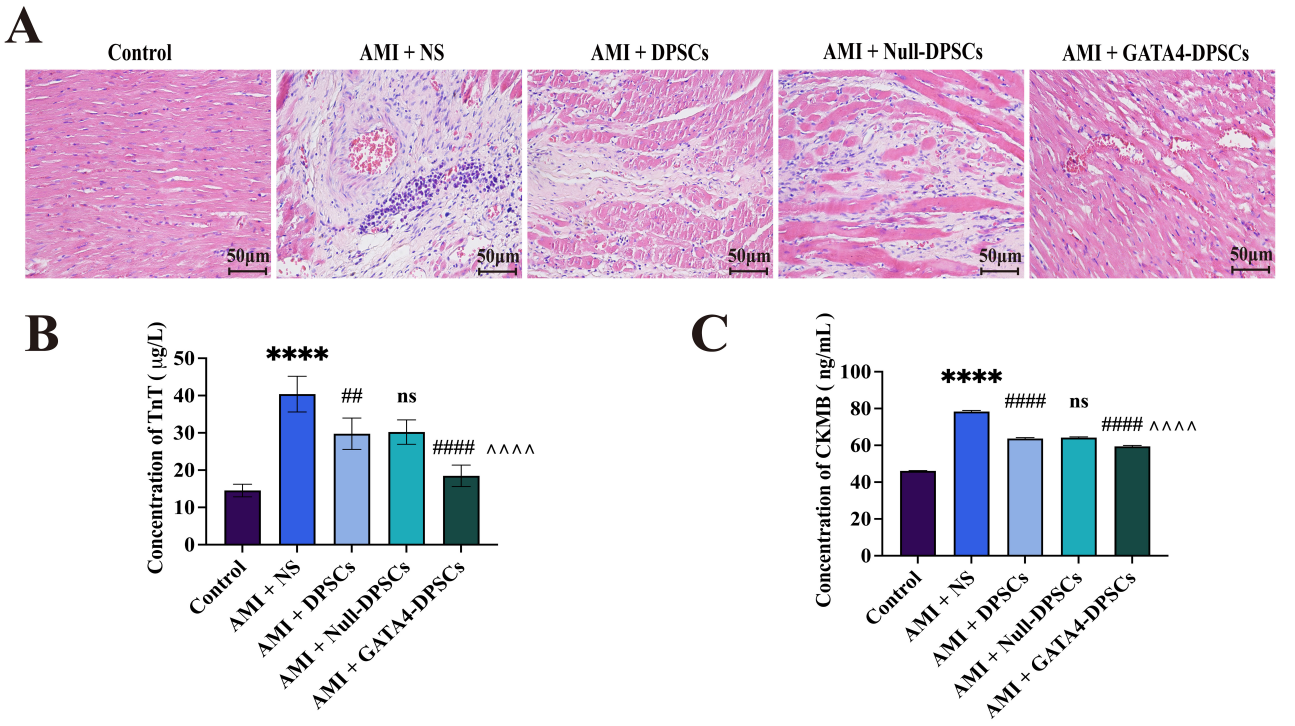

Fig. 9. Myocardial injury post-AMI. (A) Hematoxylin and eosin staining. Scale bar (A) = 50 μm. Serum TnT (B) and CKMB (C) levels. ****$p < 0.0001$ versus Control; $^{\#\#}p < 0.01$, $^{\#\#\#\#}p < 0.0001$ versus AMI + NS; $^{ns}p \geq 0.05$ versus AMI + DPSCs; $^{\wedge\wedge\wedge\wedge}p < 0.0001$ versus AMI + Null-DPSCs. $n = 6$. Abbreviations: AMI, acute myocardial infarction; CKMB, creatine kinase–myocardial band; DPSCs, dental pulp stem cells; TnT, troponin T.

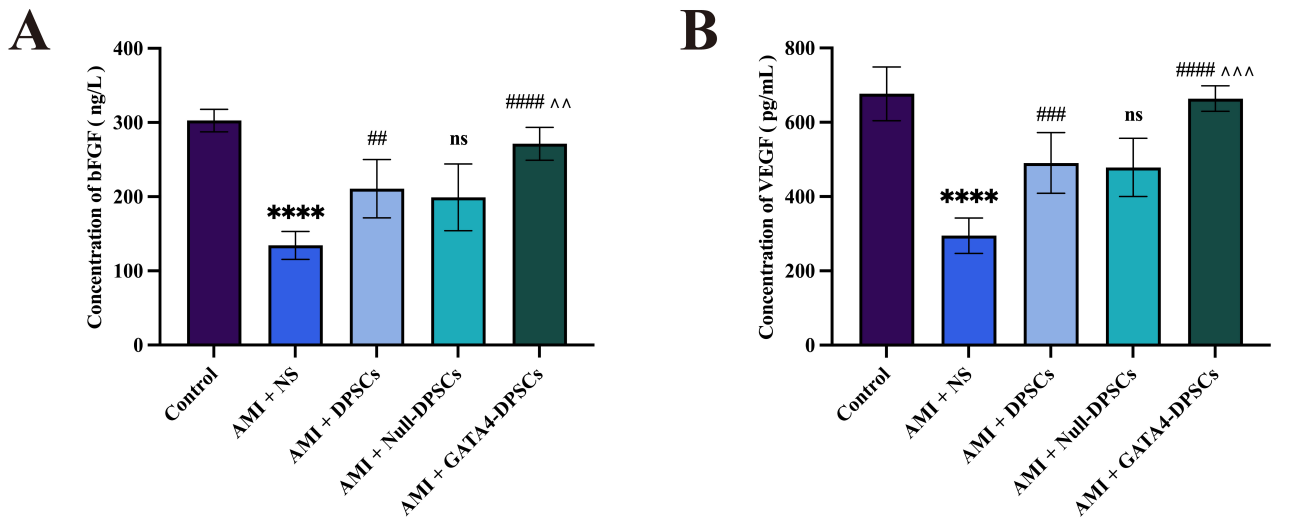

Fig. 10. Assessment of angiogenic factors in AMI rats treated with GATA4-DPSCs. Serum concentrations of bFGF (A) and VEGF (B). ****$p < 0.0001$ versus Control; $^{\#\#}p < 0.01$, $^{\#\#\#}p < 0.001$, $^{\#\#\#\#}p < 0.0001$ versus AMI + NS; $^{ns}p \geq 0.05$ versus AMI + DPSCs; $^{\wedge\wedge}p < 0.01$, $^{\wedge\wedge\wedge}p < 0.001$ versus AMI + Null-DPSCs. $n = 3$. Abbreviations: AMI, acute myocardial infarction; bFGF, basic fibroblast growth factor; DPSCs, dental pulp stem cells; VEGF, vascular endothelial growth factor.

creased expression (purple cluster), indicating attenuated fibrotic remodeling under T2 treatment (Fig. 6C). Functional enrichment analysis was performed on the intersection of DEGs between Groups T1 and C, and DEGs between Groups T2 and T1, using all expressed genes as background. Functional enrichment analysis linked the intersecting genes to collagen fibril organization and glucose metabolism (GO; Fig. 6D) and the MAPK pathway (KEGG; Fig. 6E). Full gene lists are given in **Supplementary Table 3**.

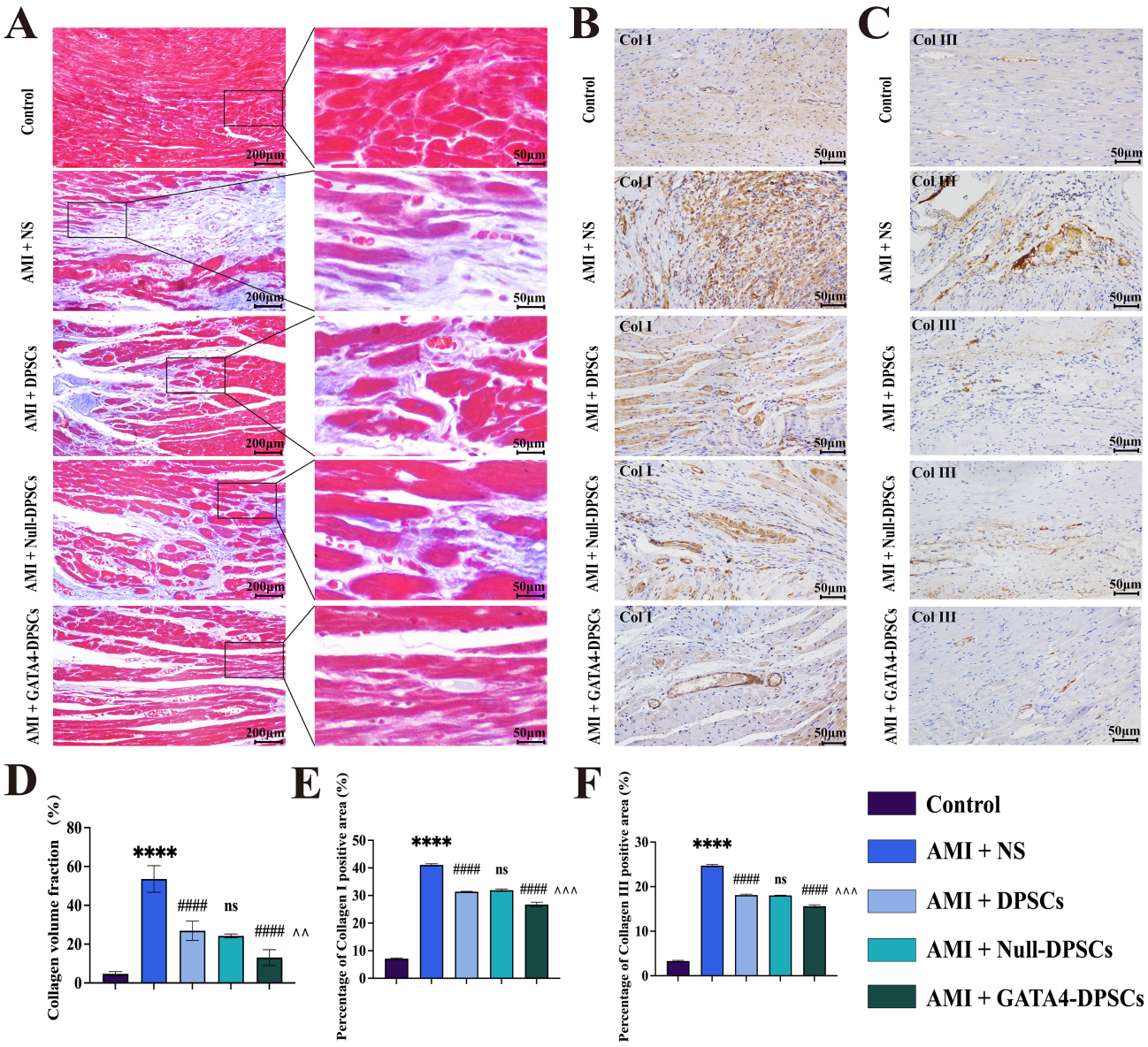

Fig. 11. Myocardial fibrosis assessment. (A) Representative Masson's trichrome staining (collagen: blue; cardiomyocytes: red). Scale bars (A) = 200 μm (main panel), 50 μm (4× magnification). (B,C) Immunohistochemical detection of collagen I (B) and collagen III (C). Scale bars (B,C) = 50 μm. (D–F) Quantitative analyses of (D) collagen volume fraction (CVF%), (E) Col I+, and (F) Col III+ areas. ****$p < 0.0001$ versus Control; $^{\#\#\#\#}p < 0.0001$ versus AMI + NS; $^{ns}p \geq 0.05$ versus AMI + DPSCs; $^{\wedge\wedge}p < 0.01$, $^{\wedge\wedge\wedge}p < 0.001$ versus AMI + Null-DPSCs. $n = 3$. Abbreviations: AMI, acute myocardial infarction; DPSCs, dental pulp stem cells.

Ex-Vivo Organ Distribution of GATA4-DPSCs in AMI Model

DiR-labeled GATA4-DPSCs were administered to AMI rats via i.p. or i.v. injection (Fig. 7A). Compared to the NC + i.v GATA4-DPSCs^{DiR} group, both injection routes in AMI rats showed significantly higher net FI values (i.p.: $p < 0.001$; i.v.: $p < 0.0001$), with i.v. delivery demonstrating superior heart homing ($p < 0.001$ versus i.p.) (Fig. 7B).

Echocardiographic Assessment of Cardiac Function of AMI Rats

Fig. 8A showed representative echocardiograms illustrating impaired cardiac function in AMI rats, as evidenced by wall motion abnormalities and chamber enlargement. Compared to the AMI + Null-DPSCs group, the AMI + GATA4-DPSCs group demonstrated significantly improved cardiac function (Fig. 8B), as evidenced by enhanced left ventricular ejection fraction (LVEF; $p < 0.01$), left ventricular fractional shortening (LVFS; $p < 0.001$), and reduced left ventricular internal diameter in systole

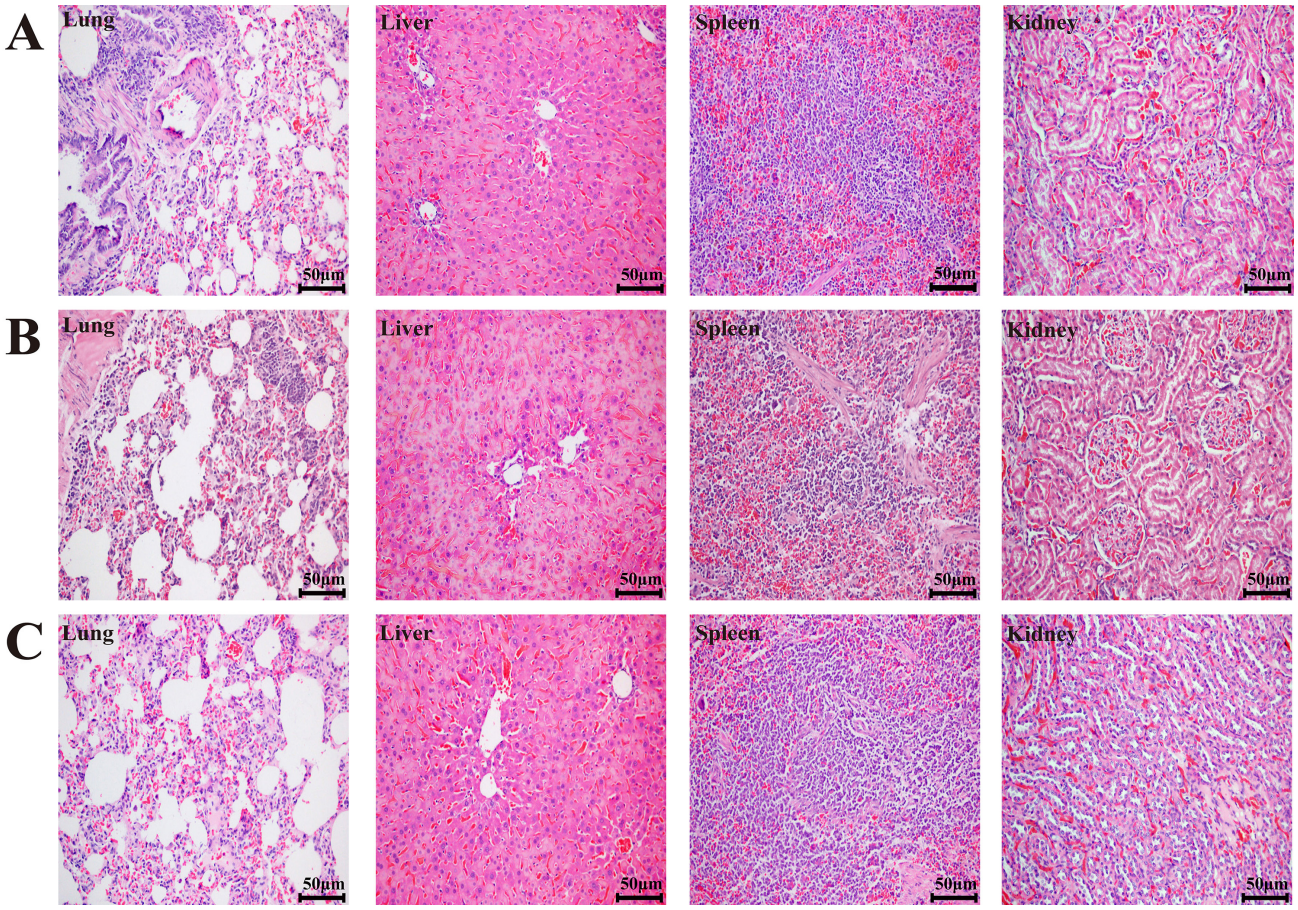

Fig. 12. Histopathological analysis of major organs. Representative HE-stained sections of lung, liver, spleen, and kidney from: (A) Control, (B) AMI + NS, and (C) AMI + GATA4-DPSCs groups. No pathological changes were observed in any of these groups. Scale bars (A,B,C) = 50 μm. Abbreviations: AMI, acute myocardial infarction; DPSCs, dental pulp stem cells; HE, hematoxylin and eosin.

(LVIDs; $p < 0.01$) and left ventricular end-systolic volume (LVESV; $p < 0.01$). Compared to the Control group, AMI induction resulted in significantly reduced Interventricular septal thickness at end-systole (IVSs; $p < 0.05$). Both DPSCs and GATA4-DPSCs transplantation treatment groups partially restored IVSs thickness relative to the AMI + NS group ($p < 0.05$, $p < 0.01$), while no significant difference was observed between the AMI + Null-DPSCs group and AMI + GATA4-DPSCs group ($p \geq 0.05$, Fig. 8B).

GATA4-DPSCs Attenuates Myocardial Injury in AMI

Histological analysis revealed severe myocardial necrosis, nuclear fragmentation, and inflammatory infiltration in the AMI + NS group, while the AMI + GATA4-DPSCs group showed markedly reduced tissue damage (Fig. 9A). TnT and CKMB were significantly attenuated by GATA4-DPSCs treatment (both $p < 0.0001$ versus Null-DPSCs; Fig. 9B,C).

GATA4-DPSCs Enhances Therapeutic Angiogenesis

As master angiogenic regulators, bFGF initiates endothelial sprouting whereas VEGF stabilizes nascent vessels—a coordination critical for revascularization [19]. All DPSCs-treated groups showed elevated bFGF and VEGF levels versus the AMI + NS group. Notably, the AMI + GATA4-DPSCs group exhibited significantly higher concentrations of both bFGF and VEGF compared to the AMI + Null-DPSCs group ($p < 0.01$, $p < 0.001$; Fig. 10A,B).

GATA4-DPSCs Attenuates Myocardial Fibrosis in AMI

Masson's trichrome staining demonstrated distinct collagen fiber distribution: the Control group exhibited predominantly red-stained myocardial fibers, while the AMI + NS group showed extensive blue collagen deposition (Fig. 11A). GATA4-DPSCs transplantation significantly reduced collagen accumulation, as quantified in terms of collagen volume fraction (CVF) ($p < 0.01$ versus AMI + Null-DPSCs group; Fig. 11D).

Compared with the AMI + Null-DPSCs group, the AMI + GATA4-DPSCs group showed a significant reduction in the percentage of collagen-positive areas for both collagen I and collagen III (both $p < 0.001$), as quantified by immunohistochemistry (Fig. 11B,C,E,F).

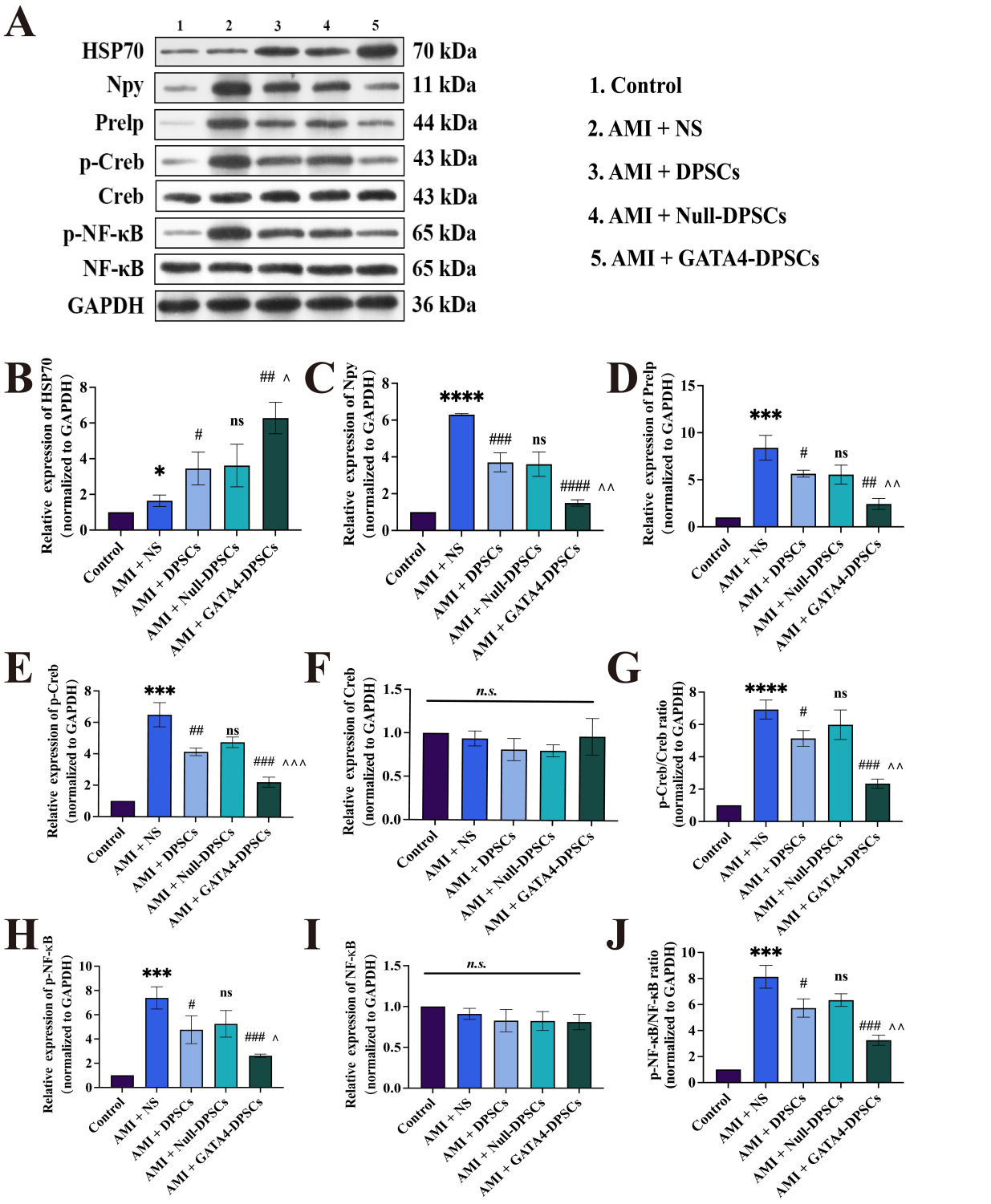

Fig. 13. Western blot analysis of key proteins in post-AMI myocardial tissue. (A) Representative immunoblots showing expression profiles of HSP70, Npy, Prelp, p-Creb, Creb, pNF-κB and NF-κB. (B–H) Quantitative densitometry analysis of protein expression levels normalized to GAPDH (loading control): (B) HSP70, (C) Npy, (D) Prelp, (E) p-Creb, (F) Creb, (G) p-Creb/Creb, (H) p-NF-κB, (I) NF-κB and (J) p-NF-κB/NF-κB. The horizontal "*n.s.*" (not significant, $p \geq 0.05$) line indicates no statistically significant differences among all five groups. *$p < 0.05$, ***$p < 0.001$, ****$p < 0.0001$ versus Control; $^{\#}p < 0.05$, $^{\#\#}p < 0.01$, $^{\#\#\#}p < 0.001$, $^{\#\#\#\#}p < 0.0001$ versus AMI + NS; $^{ns}p \geq 0.05$ versus AMI + DPSCs; $^{\wedge}p < 0.05$, $^{\wedge\wedge}p < 0.01$, $^{\wedge\wedge\wedge}p < 0.001$ versus AMI + Null-DPSCs. $n = 3$. Abbreviations: AMI, acute myocardial infarction; HSP70, heat shock protein 70; Npy, neuropeptide Y; DPSCs, dental pulp stem cells; p-Creb, phosphorylated Creb; p-NF-κB, phosphorylated nuclear factor-κB.

Comprehensive Histopathological Analysis of Major Organs

Hematoxylin and eosin (HE) staining confirmed the absence of pathological alterations (secondary infarcts or inflammatory infiltration) in lung, liver, spleen, or kidney across all experimental groups. To streamline visual presentation and enhance clarity in comparing key cohorts: Control (simulating baseline physiology), AMI + NS (simulating AMI), and AMI + GATA4-DPSCs (post-AMI therapeutic intervention)—representative HE images from these groups are selectively displayed (Fig. 12A–C).

Western Blot Verification of AMI-Associated Targets Identified by Multi-Omics Analysis

Integrated multi-omics analysis identified candidate proteins whose differential expression (**Supplementary Table 2**) was confirmed by means of Western blotting. Notably, three prioritized candidates—Hspa1b, Npy, and Prelp—were functionally linked to cardiovascular protection. The HSP70 family, including isoforms Hspa1a and Hspa1b, mitigates oxidative stress by reducing ROS accumulation [20], stabilizes calcium homeostasis, and exerts anti-apoptotic effects [21]. Npy plays pleiotropic roles in physiological processes and is upregulated in cardiovascular pathologies such as hypertension and heart failure [22,23]. Prelp has been identified to play a role in cardiac remodeling [24].

Quantification was performed for all protein bands shown in Fig. 13A. AMI induced a significant upregulation of HSP70 (detected using an antibody targeting Hspa1a, Hspa1b, and related isoforms) ($p < 0.05$; Fig. 13B). However, the AMI + GATA4-DPSCs group showed significantly elevated HSP70 levels compared to the AMI + Null-DPSCs group ($p < 0.05$; Fig. 13B). Notably, this functional outcome diverged from transcriptomic predictions, potentially reflecting the effects of either experimental duration or biological variability on stress adaptation mechanisms. Furthermore, comparative analysis demonstrated that Npy and Prelp expression peaked in the AMI + NS group, while AMI + GATA4-DPSCs transplantation significantly downregulated their expression versus AMI + Null-DPSCs group (both $p < 0.01$; Fig. 13C,D).

Western blot analysis revealed significant activation of the MAPK signaling cascade in AMI rats. Compared to the Control group, p-Creb and p-NF-κB levels were substantially elevated (both $p < 0.001$; Fig. 13E,H), with their normalized ratios (p-Creb/Creb and p-NF-κB/NF-κB) showing more pronounced increases ($p < 0.0001$ and $p < 0.001$, respectively; Fig. 13G,J). GATA4-DPSCs transplantation significantly attenuated these AMI-induced effects, reducing both phosphorylation levels (p-Creb: $p < 0.001$; p-NF-κB: $p < 0.05$ versus AMI + Null-DPSCs; Fig. 13E,H) and normalized ratios (both $p < 0.01$; Fig. 13G,J). Crucially, total Creb and NF-κB expression remained stable across groups ($p \geq 0.05$; Fig. 13F,I), confirming that the therapeutic effects specifically targeted phosphorylation-dependent activation rather than basal protein expression. These findings collectively indicate that GATA4-DPSCs mitigate post-AMI hyperactivation of MAPK-mediated transcriptional regulation through selective suppression of downstream kinase activity.

Discussion

Post-AMI myocardial fibrosis accelerates heart failure by impairing ventricular compliance and arrhythmogenicity, necessitating therapies targeting fibrotic suppression. Capitalizing on DPSCs' utility as engineered platforms [25,26] and GATA4's cardioprotective coordination via anti-apoptotic/redox pathways [27,28], we developed GATA4-overexpressing DPSCs (GATA4-DPSCs) for enhanced myocardial repair. Flow cytometry confirmed DPSC identity ($CD29^+/CD90^+/CD31^-/CD45^-$) with multilineage differentiation (osteogenic/adipogenic). According to Western blot and qPCR analyses, stable GATA4 overexpression in viable GATA4-DPSCs group conferred optimal cytoprotection in H9c2 H/R models, significantly reducing Bax while elevating Bcl-2. Critically, co-culture upregulated key cardiac functional proteins and genes in H9c2 cells: Desmin (excitation-contraction coupling [29]), Cx43 (electrophysiological synchrony [30]), *Tbx3* (electrical conduction [31]), and *Nkx2.5* (structural homeostasis [32]), indicating enhanced cardiomyocyte maturation. This coordinated regulation of apoptosis suppression and functional marker induction demonstrates GATA4-DPSCs' multifaceted protective mechanisms against ischemic injury.

Transcriptomic intersection analysis of H9c2 cells identified differential expression of *Hspa1b*, *Npy*, and *Prelp*, with functional enrichment implicating collagen infiltration and MAPK pathways. As HSP70 isoforms (Hspa1a/b) critically maintain cellular stress adaptation—where deficiency exacerbates cardiac dysfunction and MAPK/ERK-mediated Hspa1b suppression aggravates fibrosis [33]—our data indicate GATA4-DPSCs attenuate H/R injury via synergistic mechanisms: (1) upregulating HSP70 expression, (2) reducing apoptosis/oxidative stress, and (3) modulating MAPK signaling to inhibit remodeling, thus informing our *in vivo* therapeutic design.

Selection of an optimal delivery route for GATA4-DPSCs requires balancing homing efficiency, engraftment, and safety. While i.p.-administered MSCs accumulate in abdominal organs (liver/spleen) with potential peritoneal reactions [34,35], i.v. delivery demonstrates superior cardiac homing and functional recovery across ischemic models [36]. *In vivo* imaging confirmed that both i.p. and i.v. routes enabled GATA4-DPSCs homing to infarcted myocardium in AMI rats, but i.v. administration yielded significantly higher cardiac fluorescence intensity. Consequently, tail vein injection was selected to maximize myocardial targeting while minimizing adverse risks.

Echocardiographic assessment revealed GATA4-DPSCs transplantation conferred marked cardioprotection in post-infarction rats, evidenced by enhanced ventricular function (LVEF/LVFS), diminished cardiac dilation, and attenuated biomarker release (TnT, CKMB). Interestingly, both GATA4-DPSCs and Null-DPSCs transplantation comparably restored IVS thickness ($p \geq 0.05$ between groups). This comparable structural improvement suggests that: (1) DPSCs-mediated IVSs recovery primarily stems from paracrine effects common to both cell types, rather than GATA4-dependent mechanisms; and (2) the superior functional recovery (LVEF, LVFS) in the GATA4-DPSCs group likely reflects a predominantly impact on contractility rather than ventricular wall thickness. These functional improvements correspond mechanistically to neovascularization processes, wherein augmented peri-infarct microvasculature mitigates hypoxic damage through paracrine angiogenic mediators [37]. Key regulators include: FGF-driven MAPK/ERK-mediated endothelial mobilization; VEGF/VEGFR2-dependent vascular permeability and tubulogenesis [38,39]. Notably, GATA4-DPSCs administration elevated bFGF/VEGF, indicating amplified pro-angiogenic signaling and improved perfusion in border-zone ischemia. GATA4-DPSCs transplantation significantly attenuated fibrotic remodeling, as evidenced by marked reductions in CVF and fibrillar collagen deposition (collagen I and III). Histological evaluations further supported the short-term biosafety of GATA4-DPSCs, with absence of pathological inflammation or secondary infarcts in major organs (lung, liver, spleen, kidney), addressing potential concerns about systemic toxicity arising from cell therapy.

Protein profiling indicated that GATA4-DPSCs transplantation modulated the expression of HSP70, Creb, and Prelp, while suppressing MAPK signaling effectors, as evidenced by decreased p-Creb/Creb and p-NF-κB/NF-κB ratios. The MAPK signaling architecture—comprising extracellular signal-regulated kinase (ERK), p38 mitogen-activated protein kinases (p38), c-Jun N-terminal kinases (JNK), and ERK5 subfamilies—propagates extracellular stimuli through tiered phosphorylation events, inducing nuclear translocation of activated MAPKs for transcriptional control [40]. GATA4-directed MAPK modulation critically governs post-infarction repair: p38 inhibition attenuates inflammatory injury by curbing MEF2-dependent cytokine secretion (interleukin-1 beta (IL-1β)/tumor necrosis factor alpha (TNF-α)) [41,42], whereas transient JNK suppression reduces infarct size despite chronic inhibition impairing fibrotic remodeling [43]. Our findings demonstrate that GATA4-overexpressing DPSCs orchestrate multifaceted therapeutic effects on post-AMI myocardial recovery through enhanced homing to infarcted myocardium, mitigation of cardiomyocyte injury, pro-angiogenic activity, and attenuated collagen deposition. Mechanistically, these benefits converge through the synergistic MAPK pathway modulation, collectively attenuating pathological ventricular remodeling.

While the current work provides evidence for MAPK-mediated cardioprotection by GATA4-DPSCs, two critical limitations must be addressed: first, the exact downstream targets remain undefined; second, the long-term biosafety, particularly potential tumorigenic risks associated with stem cell transplantation, warrants systematic evaluation in future preclinical studies.

Conclusions

Transplantation of GATA4-overexpressing DPSCs ameliorated AMI-induced myocardial injury through synergistic cardioprotective effects—apoptosis inhibition, oxidative stress attenuation, angiogenesis potentiation, fibrosis suppression, and amelioration of ventricular remodeling—while demonstrating short-term biosafety. These benefits may be mechanistically linked to downregulation of the MAPK signaling pathway.

Availability of Data and Materials

The data are available from the corresponding author upon reasonable request.

Author Contributions

JXL and LF designed the project. JXL and YWa conducted the experiments. JXL and YWu drafted the manuscript, and analyzed sequencing data. JXL and YHD disposed of data and provided valuable advice. All authors were involved in the critical revision of the manuscript. All authors have read and approved the final manuscript. All authors have participated sufficiently in the work and agreed to be accountable for all aspects of the work.

Ethics Approval and Consent to Participate

Approval was granted by the Ethics Committee of The First Affiliated Hospital of Harbin Medical University (Date:10/15/2021. No:2021133).

Acknowledgment

Not applicable.

Funding

This research received no external funding.

Conflict of Interest

The authors declare no conflict of interest.

Supplementary Material

Supplementary material associated with this article can be found, in the online version, at https://doi.org/10.24976/Discov.Med.202537199.146.

References

[1] Zhao D, Liu J, Wang M, Zhang X, Zhou M. Epidemiology of cardiovascular disease in China: current features and implications. Nature Reviews. Cardiology. 2019; 16: 203–212. https://doi.org/10.1038/s41569-018-0119-4.

[2] Timmis A, Townsend N, Gale CP, Torbica A, Lettino M, Petersen SE, *et al*. European Society of Cardiology: Cardiovascular Disease Statistics 2019. European Heart Journal. 2020; 41: 12–85. https://doi.org/10.1093/eurheartj/ehz859.

[3] Virani SS, Alonso A, Benjamin EJ, Bittencourt MS, Callaway CW, Carson AP, *et al*. Heart Disease and Stroke Statistics-2020 Update: A Report From the American Heart Association. Circulation. 2020; 141: e139–e596. https://doi.org/10.1161/CIR.0000000000000757.

[4] Sui B, Wu D, Xiang L, Fu Y, Kou X, Shi S. Dental Pulp Stem Cells: From Discovery to Clinical Application. Journal of Endodontics. 2020; 46: S46–S55. https://doi.org/10.1016/j.joen.2020.06.027.

[5] Gronthos S, Mankani M, Brahim J, Robey PG, Shi S. Postnatal human dental pulp stem cells (DPSCs) in vitro and in vivo. Proceedings of the National Academy of Sciences of the United States of America. 2000; 97: 13625–13630. https://doi.org/10.1073/pnas.240309797.

[6] Zhang Z, Shayani G, Xu Y, Kim A, Hong Y, Feng H, *et al*. Induction of Senescence by Loss of Gata4 in Cardiac Fibroblasts. Cells. 2023; 12: 1652. https://doi.org/10.3390/cells12121652.

[7] Jurado Acosta A, Rysä J, Szabo Z, Moilanen AM, Serpi R, Ruskoaho H. Phosphorylation of GATA4 at serine 105 is required for left ventricular remodelling process in angiotensin II-induced hypertension in rats. Basic & Clinical Pharmacology & Toxicology. 2020; 127: 178–195. https://doi.org/10.1111/bcpt.13398.

[8] Yang JJ, Zhang XH, Ma XH, Duan WJ, Xu NG, Chen YJ, *et al*. Astragaloside IV enhances GATA-4 mediated myocardial protection effect in hypoxia/reoxygenation injured H9c2 cells. Nutrition, Metabolism, and Cardiovascular Diseases: NMCD. 2020; 30: 829–842. https://doi.org/10.1016/j.numecd.2020.01.009.

[9] Song R, Lei H, Feng L, Cheng W, Li Y, Yao LL, *et al*. TFEB insufficiency promotes cardiac hypertrophy by blocking autophagic degradation of GATA4. The Journal of Biological Chemistry. 2021; 297: 101189. https://doi.org/10.1016/j.jbc.2021.101189.

[10] Haridhasapavalan KK, Sundaravadivelu PK, Bhattacharyya S, Ranjan SH, Raina K, Thummer RP. Generation of cell-permeant recombinant human transcription factor GATA4 from E. coli. Bioprocess and Biosystems Engineering. 2021; 44: 1131–1146. https://doi.org/10.1007/s00449-021-02516-8.

[11] Thygesen K, Alpert JS, Jaffe AS, Chaitman BR, Bax JJ, Morrow DA, *et al*. Fourth Universal Definition of Myocardial Infarction (2018). Journal of the American College of Cardiology. 2018; 72: 2231–2264. https://doi.org/10.1016/j.jacc.2018.08.1038.

[12] Dominici M, Le Blanc K, Mueller I, Slaper-Cortenbach I, Marini F, Krause D, *et al*. Minimal criteria for defining multipotent mesenchymal stromal cells. The International Society for Cellular Therapy position statement. Cytotherapy. 2006; 8: 315–317. https://doi.org/10.1080/14653240600855905.

[13] Kern S, Eichler H, Stoeve J, Klüter H, Bieback K. Comparative analysis of mesenchymal stem cells from bone marrow, umbilical cord blood, or adipose tissue. Stem Cells (Dayton, Ohio). 2006; 24: 1294–1301. https://doi.org/10.1634/stemcells.2005-0342.

[14] Bellaver B, Povala G, Ferreira PCL, Ferrari-Souza JP, Leffa DT, Lussier FZ, *et al*. Astrocyte reactivity influences amyloid-β effects on tau pathology in preclinical Alzheimer's disease. Nature Medicine. 2023; 29: 1775–1781. https://doi.org/10.1038/s41591-023-02380-x.

[15] Gunawan I, Kohane FV, Dey M, Nguyen K, Zheng Y, Neumann DP, *et al*. Extensible Immunofluorescence (ExIF) accessibly generates high-plexity datasets by integrating standard 4-plex imaging data. Nature Communications. 2025; 16: 4606. https://doi.org/10.1038/s41467-025-59592-7.

[16] Wang L, Liu YQ, Gu QX, Zhang C, Xu L, Wang L, *et al*. Serum N-Glycan Markers for Diagnosing Significant Liver Fibrosis and Cirrhosis in Chronic Hepatitis B Patients with Normal Alanine Aminotransferase Levels. Engineering. 2023; 26: 151–158. https://doi.org/10.1016/j.eng.2023.03.008.

[17] Wang SS, Liu ZK, Liu JJ, Cheng Q, Wang YX, Liu Y, *et al*. Imaging asparaginyl endopeptidase (AEP) in the live brain as a biomarker for Alzheimer's disease. Journal of Nanobiotechnology. 2021; 19: 249. https://doi.org/10.1186/s12951-021-00988-0.

[18] Papaioannou I, Dritsoula A, Kang P, Baliga RS, Trinder SL, Cook E, *et al*. NKX2-5 regulates vessel remodeling in scleroderma-associated pulmonary arterial hypertension. JCI Insight. 2024; 9: e164191. https://doi.org/10.1172/jci.insight.164191.

[19] Carmeliet P, Jain RK. Molecular mechanisms and clinical applications of angiogenesis. Nature. 2011; 473: 298–307. https://doi.org/10.1038/nature10144.

[20] Chen Z, Shen X, Shen F, Zhong W, Wu H, Liu S, *et al*. TAK1 activates AMPK-dependent cell death pathway in hydrogen peroxide-treated cardiomyocytes, inhibited by heat shock protein-70. Molecular and Cellular Biochemistry. 2013; 377: 35–44. https://doi.org/10.1007/s11010-013-1568-z.

[21] Choudhury S, Bae S, Ke Q, Lee JY, Kim J, Kang PM. Mitochondria to nucleus translocation of AIF in mice lacking Hsp70 during ischemia/reperfusion. Basic Research in Cardiology. 2011; 106: 397–407. https://doi.org/10.1007/s00395-011-0164-1.

[22] Qin YY, Huang XR, Zhang J, Wu W, Chen J, Wan S, *et al*. Neuropeptide Y attenuates cardiac remodeling and deterioration of function following myocardial infarction. Molecular Therapy: the Journal of the American Society of Gene Therapy. 2022; 30: 881–897. https://doi.org/10.1016/j.ymthe.2021.10.005.

[23] Medzikovic L, van Roomen C, Baartscheer A, van Loenen PB, de Vos J, Bakker ENTP, *et al*. Nur77 protects against adverse cardiac remodelling by limiting neuropeptide Y signalling in the sympathoadrenal-cardiac axis. Cardiovascular Research. 2018; 114: 1617–1628. https://doi.org/10.1093/cvr/cvy125.

[24] Barallobre-Barreiro J, Didangelos A, Schoendube FA, Drozdov I, Yin X, Fernández-Caggiano M, *et al*. Proteomics analysis of cardiac extracellular matrix remodeling in a porcine model of ischemia/reperfusion injury. Circulation. 2012; 125: 789–802. https://doi.org/10.1161/CIRCULATIONAHA.111.056952.

[25] Chen Y, Wang X, Wu Z, Jia S, Wan M. Epigenetic regulation of dental-derived stem cells and their application in pulp and periodontal regeneration. PeerJ. 2023; 11: e14550. https://doi.org/10.7717/peerj.14550.

[26] Yamaza T, Kentaro A, Chen C, Liu Y, Shi Y, Gronthos S, *et al*. Immunomodulatory properties of stem cells from human exfoliated deciduous teeth. Stem Cell Research & Therapy. 2010; 1: 5. https://doi.org/10.1186/scrt5.

[27] Kobayashi S, Lackey T, Huang Y, Bisping E, Pu WT, Boxer LM, *et al*. Transcription factor gata4 regulates cardiac BCL2

gene expression in vitro and in vivo. FASEB Journal: Official Publication of the Federation of American Societies for Experimental Biology. 2006; 20: 800–802. https://doi.org/10.1096/fj.05-5426fje.

[28] Shan X, Xu X, Cao B, Wang Y, Guo L, Zhu Q, *et al*. Transcription factor GATA-4 is involved in erythropoietin-induced cardioprotection against myocardial ischemia/reperfusion injury. International Journal of Cardiology. 2009; 134: 384–392. https://doi.org/10.1016/j.ijcard.2008.03.043.

[29] Singh SR, Kadioglu H, Patel K, Carrier L, Agnetti G. Is Desmin Propensity to Aggregate Part of its Protective Function? Cells. 2020; 9: 491. https://doi.org/10.3390/cells9020491.

[30] Martins-Marques T, Witschas K, Ribeiro I, Zuzarte M, Catarino S, Ribeiro-Rodrigues T, *et al*. Cx43 can form functional channels at the nuclear envelope and modulate gene expression in cardiac cells. Open Biology. 2023; 13: 230258. https://doi.org/10.1098/rsob.230258.

[31] Delisle BP, Yu Y, Puvvula P, Hall AR, Huff C, Moon AM. Tbx3-Mediated Regulation of Cardiac Conduction System Development and Function: Potential Contributions of Alternative RNA Processing. Pediatric Cardiology. 2019; 40: 1388–1400. https://doi.org/10.1007/s00246-019-02166-4.

[32] Gou D, Zhou J, Song Q, Wang Z, Bai X, Zhang Y, *et al*. Mog1 knockout causes cardiac hypertrophy and heart failure by down-regulating tbx5-cryab-hspb2 signalling in zebrafish. Acta Physiologica (Oxford, England). 2021; 231: e13567. https://doi.org/10.1111/apha.13567.

[33] Tao H, Xu W, Qu W, Gao H, Zhang J, Cheng X, *et al*. Loss of ten-eleven translocation 2 induces cardiac hypertrophy and fibrosis through modulating ERK signaling pathway. Human Molecular Genetics. 2021; 30: 865–879. https://doi.org/10.1093/hmg/ddab046.

[34] Song WJ, Li Q, Ryu MO, Ahn JO, Bhang DH, Jung YC, *et al*. TSG-6 released from intraperitoneally injected canine adipose tissue-derived mesenchymal stem cells ameliorate inflammatory bowel disease by inducing M2 macrophage switch in mice. Stem Cell Research & Therapy. 2018; 9: 91. https://doi.org/10.1186/s13287-018-0841-1.

[35] García Gómez-Heras S, García-Arranz M, Vega-Clemente L, Olivera-Salazar R, Vélez Pinto JF, Fernández-García M, *et al*. Study of the Effect of Wild-Type and Transiently Expressing CXCR4 and IL-10 Mesenchymal Stromal Cells in a Mouse Model of Peritonitis. International Journal of Molecular Sciences. 2023; 25: 520. https://doi.org/10.3390/ijms25010520.

[36] Szydlak R. Mesenchymal stem cells' homing and cardiac tissue repair. Acta Biochimica Polonica. 2019; 66: 483–489. https://doi.org/10.18388/abp.2019_2890.

[37] Folkman J. Angiogenesis in cancer, vascular, rheumatoid and other disease. Nature Medicine. 1995; 1: 27–31. https://doi.org/10.1038/nm0195-27.

[38] Presta M, Dell'Era P, Mitola S, Moroni E, Ronca R, Rusnati M. Fibroblast growth factor/fibroblast growth factor receptor system in angiogenesis. Cytokine & Growth Factor Reviews. 2005; 16: 159–178. https://doi.org/10.1016/j.cytogfr.2005.01.004.

[39] Shibuya M. Vascular endothelial growth factor and its receptor system: physiological functions in angiogenesis and pathological roles in various diseases. Journal of Biochemistry. 2013; 153: 13–19. https://doi.org/10.1093/jb/mvs136.

[40] Cargnello M, Roux PP. Activation and function of the MAPKs and their substrates, the MAPK-activated protein kinases. Microbiology and Molecular Biology Reviews: MMBR. 2011; 75: 50–83. https://doi.org/10.1128/MMBR.00031-10.

[41] Liang Q, Bueno OF, Wilkins BJ, Kuan CY, Xia Y, Molkentin JD. c-Jun N-terminal kinases (JNK) antagonize cardiac growth through cross-talk with calcineurin-NFAT signaling. The EMBO Journal. 2003; 22: 5079–5089. https://doi.org/10.1093/emboj/cdg474.

[42] Tang W, Wei Y, Le K, Li Z, Bao Y, Gao J, *et al*. Mitogen-activated protein kinases ERK 1/2- and p38-GATA4 pathways mediate the Ang II-induced activation of FGF2 gene in neonatal rat cardiomyocytes. Biochemical Pharmacology. 2011; 81: 518–525. https://doi.org/10.1016/j.bcp.2010.11.012.

[43] ZHsieh YL, Tsai YL, Shibu MA, Su CC, Chung LC, Pai P, *et al*. ZAK induces cardiomyocyte hypertrophy and brain natriuretic peptide expression via p38/JNK signaling and GATA4/c-Jun transcriptional factor activation. Molecular and Cellular Biochemistry. 2015; 405: 1–9. https://doi.org/10.1007/s11010-015-2389-z.